Constraining supernova progenitors with integral field spectroscopy

Master's Thesis
University of Turku
Dept. of Physics and Astronomy
Astronomy
September 2019
BSc Timo Kravtsov
Supervised by:
Dr. Hanindyo Kuncarayakti
Prof. Seppo Mattila

The originality of this thesis has been checked in accordance with the University of Turku quality assurance system using the Turnitin OriginalityCheck service.

UNIVERSITY OF TURKU
Department of Physics and Astronomy
KRAVTSOV, TIMO: Constraining supernova progenitors with integral field spectroscopy
Master's thesis, 57 p.
Astronomy
September 2019

Core-collapse supernovae (CCSNe) are an important part of the stellar evolution of massive stars. Certain types of supernova (SN) explosions are believed to originate from similar types of stars, but linking a SN type directly to a progenitor star has proven to be a challenge. A powerful way to study SN progenitors is to directly observe the star before the explosion, but only a handful of such stars have been observed to date.

Stripped-envelope SNe includes types Ib, Ic, IIb and Ibn. Type Ibn supernovae are not well understood. The spectral evolution shows the SN ejecta interacting with helium-rich circumstellar material (CSM). The progenitors are thought to be Wolf-Rayet stars that have lost part of their helium envelope through strong stellar winds or binary systems where the CSM is produced through binary interaction. Similarly type IIb SNe show evidence of depleted hydrogen envelopes, but still retaining small amount of hydrogen on the surface layer. Previously, some evidence has been presented that the progenitors of type Ib and type Ic SNe could be classical Wolf-Rayet stars or lower mass stars in binary systems, but more studies are needed to understand them.

In this thesis, I have studied the properties of the environments of several SNe, including a type Ibn, a type IIb, a type Ia and one unknown transient, and their host galaxy NGC 2466 using VLT/MUSE, an integral field spectrograph. Properties such as supernova environment's age and metallicity were measured and compared to the measurements of the whole galaxy using statistical methods. The age was inferred by fitting spectra of the supernova environments with simple stellar population models and by comparing the observed emission lines to photoionisation models. The results suggest an interacting binary system to be the most likely progenitor for both of the studied stripped-envelope supernovae.

Keywords: Supernovae, supernova progenitors, core-collapse supernovae, thermonuclear supernovae, MUSE instrument, binary stars, Wolf-Rayet stars, simple stellar population, BPASS models

Contents

1 Introduction

SNe are the final death throes of stars, momentarily outshining their host galaxy.

Supernovae (SNe) are spectroscopically divided into two general classes; type I SNe are missing spectral lines from hydrogen while type II SNe have hydrogen lines visible. These classes are then divided into sub-classes; type Ia SNe have strong silicon absorption lines, type Ib SNe have helium lines whereas type Ic do not.[1] Differentiating type Ib and type Ic SNe can be challenging, so they are often listed together as type Ibc.[2] Transitional SNe between types II and Ib also exist, dubbed type IIb. They appear as type II SNe in early times but transition to a type Ib in later times.[3] Recently a new and rare type of SNe has been discovered; type Ibn. They have narrower emission lines of helium than usual in their spectra, which is also a contrast to type Ib SNe where helium lines are in absorption. This indicates the presence of cool He-rich circumstellar matter (CSM). A prototype SN for this type is SN 2006jc.[4, 5, 6]

Type Ia SNe are believed to originate from white dwarf stars in binary systems, where the white dwarf accretes mass from its companion through Roche-lobe overflow.[7] A white dwarf is a remnant of a low mass star that is supported from collapse by electron degeneracy pressure. In a type Ia SN explosion star reaches a mass near the Chandrasekhar limit, 1.4 $M_\odot$, where 1 $M_\odot$ corresponds to a solar mass of $1.989 \cdot 10^{30}$ kg. This limit is the maximum mass that a white dwarf can support without collapsing. After accreting sufficient amount of material from a companion, the star then undergoes a fast and violent thermonuclear fusion reaction disintegrating the whole star.[8] In these SNe, the relationship between peak brightness and the brightness decline rate have been found to be strongly coupled. They can therefore be used in cosmology as standard candles for distance measurements.[9] Alternatively a type Ia SN can be produced from a double white dwarf system where the two star remnants merge and explode if the total mass after merger is equiv-

alent or higher than the Chandrasekhar mass.[10] The ages estimated for type Ia SN progenitors also show two distinct groups. The first channel has delay times less than 400 Myr after formation and the second channel over 2.4 Gyr.[11] White dwarfs themselves are produced by stars with masses lower than 8 $M_{\odot}$.

The rest of the SN types are interpreted as CCSNe. The progenitor star initial masses are higher than 8 $M_{\odot}$.[1] At the end of the progenitor star's lifetime it has spent all of its fusionable fuel in the core and the star collapses under its own gravity. The increasing core pressure causes protons to capture electrons, producing neutrons and electron neutrinos. The pressure from the falling outer layers is not enough to overcome the neutron degeneracy pressure and the outer layers rebound from the surface of the forming neutron core. The rebound would quickly stall, but a small fraction of neutrinos produced in the neutron core deposit additional energy to the rebounding matter. The neutrino reheating gives the matter enough energy to become gravitationally unbound and the star explodes as a supernova. In this scenario the SN leaves behind a neutron star. At certain masses some of the material fall back on the surface of the newly formed neutron star, collapsing into a black hole. It is also possible that the neutrino reheating fails to deposit enough energy to the outer layers and the supernova fails completely. In these cases a black hole is believed to be formed without a significant explosion.[12, 13, 14]

The theory behind the spectral classification of CCSNe is as follows. The progenitors are layered with different elements like onion shells and with heavier elements forming toward the core. Type II SNe still show signs of hydrogen present in their spectra, which means that there is still a considerable amount of hydrogen in the outermost layer of the star. This means they are still mostly intact at the moment of explosion. This is a contrast to Ibc SNe, where the spectral information indicates that hydrogen or even helium layers have been stripped from the stellar surface. The intermediate type IIb SN has only a thin layer of hydrogen on the progenitor

surface and as deeper layers of the ejecta are revealed, the helium layer becomes visible and the SN transitions to type Ib. The progenitors of type II SNe have also been identified to be red supergiants through direct imaging before the supernova event.[15, 3]

Type II SNe are divided into its own subcategories. type IIP SNe have a plateau in their light curves where the brightness stays nearly constant for several months. Type IIL SNe have a roughly linear relationship between magnitude and time, getting dimmer over time after the peak brightness. Type IIn SNe have unusually narrow and bright hydrogen lines present, hinting the presence of a dense and slow-moving CSM around the star.

Type Ibc SN progenitors are traditionally thought to be Wolf-Rayet (WR) type stars. They are massive stars with a minimum Zero-Age Main Sequence Mass (ZAMS) of 25 $M_\odot$ at solar metallicity and increasing in minimum mass when lowering metallicity.[16] They are also extremely short-lived with a longest possible age of about 5 Myrs. WR stars also exhibit strong stellar winds and mass loss, typical mass loss rates being in the order of $\dot{M}_\odot \sim 10^{-5}$ $M_\odot$/yr. The stellar wind is caused by metals in the stellar atmosphere, which transfer photon energy into momentum through absorption. Such winds are used to explain the interpreted missing outer layers of hydrogen or helium in the progenitors. WR stars are spectroscopically differentiated into subcategories according to the observed emission lines originating from the stellar atmosphere. In a type Ibn SN it is believed that the SN ejecta collide with a relatively slow moving helium-rich CSM, converting the kinetic energy into light, producing the narrow helium emission lines. The full width at half maximum (FWHM) of these lines are from few hundred to few thousand km/s.[5]

However, the frequency of observed type Ibc SNe is more than what the estimated size of the WR population allows, so an alternative production channel for these SNe is required.[12] Most of the stars in the Universe are in binary systems.[17] In some

of these systems the components are close enough to interact with each other.[18] Through interaction it is possible that one of the components is stripped of its outer layers to produce a WR-like star. This channel would allow stripped-envelope SN progenitors to have a lower initial mass and therefore be more numerous.[19]

The obvious way to identify a progenitor of a SN is to directly image the progenitor before the explosion. This has been done a few times for a type IIP SN and the progenitor in these cases have most often been identified as a red supergiant with a relatively low initial mass.[20, 21] The main problem with this method is the limited availability of images of host galaxies before the explosion. This method requires a good angular resolution and proximity for the host, because the progenitor star needs to be resolved from other stars. This limits observations to the Hubble Space Telescope and the largest ground-based telescopes to a distance of about 20 Mpc.[22]

In this thesis I study a SN host galaxy NGC 2466 using an integral field spectrograph (IFS). The galaxy has hosted three confirmed SNe; ASASSN-14dd, SN 2016iye and SN 2003gh. Their spectral classifications are type Ibn, IIb and Ia, respectively. Additionaly there is a fourth unclassified transient, AT 2016cnz. With the excellent spatial resolution of VLT/MUSE and the proximity of the host galaxy, a redshift of z=0.0178 translates into a comoving distance of 76.4 Mpc, it is possible to resolve regions down to few hundred parsecs, scale of 364 pc/", making the study of immediate SNe environments possible. These regions can be compared to other regions or the galaxy as a whole. Also, from the measurements of the SN environments constraints on to the progenitors can be determined. In Chapter 2, I will go over previous studies on SN progenitors and derived constraints. In Chapter 3, I will present the instrument, data and reduction methods used in this study. In Chapter 4, I will introduce all the different methods used for the data analysis. In Chapter 5, I will present and discuss the results of this study. In Chapter 6, I will present my conclusions on based these results.

2 Previous studies on supernova environments and progenitors

The view that type Ibc SNe are caused by solitary WR stars has been challenged in recent years. Stars are born with a range of masses from a fraction of a solar mass up to hundreds of solar masses. Initial mass function describes the number density of stars for a given initial stellar mass in a stellar population. In all initial mass functions, e.g. Salpeter (1955)[23], the number of lower mass stars is higher than high mass stars in a given recently formed stellar population. From these numbers a theoretical ratio of type Ibc/type II SNe can be predicted, but observations reveal a higher number of type Ibc SNe than expected.[12] The high observed number ratio of type Ibc/type II SNe requires an additional progenitor channel to explain it. Interacting binary systems have been suggested as an alternative method to produce these stripped-envelope SNe. In these type of binaries the outer layers of a component star are stripped by the other component through Roche-lobe overflow. The resulting star has no hydrogen in it and resembles a solitary WR star, but with a lower initial mass. In a recent study Shivvers et al. (2017)[24] examined the nearby type Ibn SN, SN2015G. With a previous photometric nondetection of the progenitor they could constrain an upper limit of 18 $M_{\odot}$ for the progenitor ZAMS. This low mass indicates that the progenitor simply cannot be a single WR star. Additionally Eldridge et al. (2013)[25] show that not all type Ibc progenitors can be massive WR stars.

Alternative method for constraining the progenitor properties is to study the general environment of the SNe. CCSN progenitors are short-lived stars with ages ranging 5-40 Myrs.[26] Typical velocity dispersion for stars in a cluster is a few pc/Myr.[27] It is thus safe to assume that the progenitor and the immediate surrounding region, i.e. unresolved stellar population at the SN position, are still

coupled. The stars in the local population have likely been formed at the same time, sharing the same age and metallicity.[28] Optimally, the host galaxy is nearby enough that for example the young H II region where the SN was located can be resolved from other parts of the host galaxy.

One important and basic method of environment study is to measure the Hα flux of regions in a host galaxy. Hα emission is produced by recombinging hydrogen atoms. These atoms are ionised by photons from short-lived massive stars so Hα maps out star forming regions. The galaxy is imaged using a Hα filter and the pixels are ranked in a normalized cumulative rank (NCR) function.[29, 30] Brightest pixels in the galaxy have a value of 1 while the background sky has a value of 0. Because Hα can be used to trace out the younger regions in a galaxy, this gives an age constraint for a SN progenitor.[31] With a large sample of different types of SNe it can be studied if there is a significant age difference for the environments of SN types and if the types are associated with certain age ranges.

Radial distance from the host nucleus is another method to study the environments. Spiral galaxies in general have a metallicity gradient in their disks, with high metallicity near to the nucleus and decreasing steadily outward.[32] This is especially important with WR progenitors as the stellar wind strength is strongly linked to the metallicity of the star.[33] The tendency for stripped-envelope SNe to be more likely located in the inner parts of the host galaxy has been observed by Hakobyan et al. (2009)[34]and Habergham et al.[35].

Because of the short lifespans of CCSNe progenitors and the fact that the metallicity of the H II region and the massive stars in it are similar, measuring the interstellar medium (ISM) metallicity will in fact indirectly measure the metallicity of the progenitor.

3 Data acquisition and reduction

The Very Large Telescope (VLT) of the European Southern Observatory (ESO) is located in Paranal, Chile and was completed in 2000. It is composed of four telescopes with primary mirrors of 8.2 meters in diameter each and with a Ritchey–Chrétien design. The site has generally excellent seeing, the full width at half maximum (FWHM) of a typical night being under 0.7".[36] MUSE (Multi Unit Spectroscopic Explorer) is an integral field spectrograph (IFS) mounted on the VLT's fourth telescope, called UT4 or Yepun. An IFS is an instrument which simultaneously acquires spectral data over a field of view (FoV) on the sky. MUSE's FoV in wide field mode is 1'x1' and it produces spectra for each of its roughly 300x300 pixels in the image. This is done by slicing the FoV to 24 parts, which are then moved to 24 individual IFS sub-systems, where the slices are divided into 48 separate sub-regions and run through a spectroscope. Each of these regions, shown in Figure 1, correspond to about 75 spaxels in the final datacube. The default final products are a datacube with spectral information for each pixel and a collapsed image of the whole region. One pixel in the image corresponds to 0.2" in the sky. Spatial pixels, usually abbreviated as spaxels, contain spectra with range from 4750 Å to 9350 Å in the instrument's nominal spectral mode. The instrument also offers an extended mode where the spectral range starts from 4600 Å, but suffers from second order contaminations from 8500 Å onwards. MUSE's spectral resolution varies from R = 1770 to R = 3590 linearly almost through the whole wavelength range. Spectral resolution is defined as

$$R = \frac{\lambda}{\Delta\lambda}, \tag{1}$$

where $\Delta\lambda$ is the smallest observable wavelength difference around the wavelength λ. Spectral resolution is R = 2500 at the Hα wavelength of 6562 Å. The wavelength range is sampled at constant 1.25 Å bins through the whole wavelength range. The main science goals of MUSE are in the fields of high redshift galaxies and other

extended objects, where spatial samplings of spectra is needed. The All-weather MUse Supernova Integral-field Nearby Galaxies survey[1] has observed low redshift SN host galaxies and the data in this thesis is part of that project.[37, 38]

3.1 Observations

NGC 2466 is a spiral galaxy located at R.A. = 07h45m15.963s Dec = -71°24'37.63" with recessional velocity of cz = 5376 km/s.[39, 40] In this thesis a redshift of z = 0.0178 was measured. The angular scale of the galaxy is 364 pc/", assuming a distance of 76.4 Mpc. The galaxy has hosted three observed SNe between years 2003 and 2016, with an additional transient object in 2016. The three SNe, SN 2003gh, ASASSN-14dd and SN 2016iye, were identified to be of types Ia[2], Ibn[3] and IIb[4], respectively. No follow-up observations were conducted on the second 2016 transient, AT 2016cnz, and its nature is unknown. ASASSN-14dd was the main motivation for the MUSE observation, but through serendipity other SN sites are also available for study in the same observation.

The galaxy was observed with MUSE on December of 2015, on the nights of 10th, 27th and 28th. Reported DIMM[5] seeing was between 0.8" and 2" with thin clouds during some of the observation nights. The galaxy is roughly 2' in diameter and to capture the full galaxy, the observation was conducted with four pointings and four exposures with each pointing. Between exposures the FoV was rotated by 90° and dithered by few arc seconds to minimize systematic errors due to the instrument. The exposure times were 698s for each shot, totaling 11168s to cover

[1] AMUSING is a survey that has observed over 350 SN host galaxies with MUSE over the past few years. Principal investigators are Anderson J., Galbany L. and Kuncarayakti H.

[2] https://wis-tns.weizmann.ac.il/object/2003gh

[3] http://www.astronomerstelegram.org/?read=6293

[4] http://www.astronomerstelegram.org/?read=9886

[5] Differential Image Motion Monitor uses two simultaneous images of the same star that were taken through a different columns of air to estimate the seeing conditions.

the whole galaxy. Effective exposure time is therefore 2792s for spaxels over the whole galaxy.

3.2 Data reduction

Raw exposure from MUSE is a multi-extension FITS frame including exposures from each of the 24 IFSs. It also contains logs of the pointing accuracy and corrections, and information on the variation in the seeing during the exposure.

Data are reduced by running them through the MUSE recipe package version 2.0.3., executed with a program called ESO Recipe Execution Tool (EsoRex). Additionally there exists a graphical user interface for EsoRex called EsoReflex[1].[41] Its usage is recommended because the amount of data handled is unusually large compared to other instruments, but exactly the same results are gained by manually running recipes from the command line[2].

First recipe to be executed is **muse_bias**. The recipe takes 11 (minimum of three) bias exposures taken on the same day and produces one master bias file for the night. The images have a zero exposure time and are used to remove the artificial signal addition to each pixel. This addition is done to ensure that the electron counts in a pixel is always positive. As with all the proceeding master calibration files, the master bias is also a multi-extension FITS file with separate bias images for each IFS. Master bias is subtracted from all other exposures done during the night.

Normally all the images are subtracted by a dark image, which is produced by taking an image with the instrument with an exposure time similar to the actual observation, but with a closed shutter. This removes the inherent instrument thermal noise. Though dark images are taken periodically with MUSE and are available for use, it is not recommended to use them. MUSE has a very small thermal noise and trying to remove it will most likely only add noise to the final images.

[1]https://www.eso.org/sci/software/esoreflex/

[2]Resources from Finnish IT Center for Science were used for the reduction process.

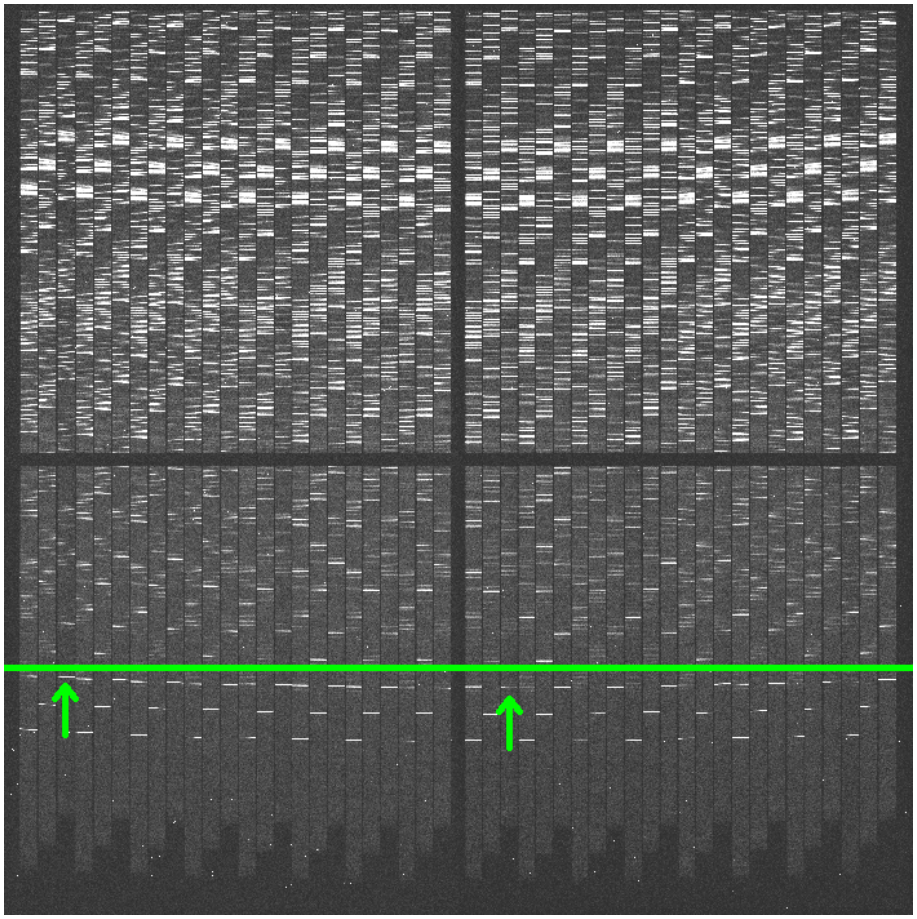

Figure 1. Example raw spectra from one of the IFSs within MUSE. Exposure taken is of an arc lamp. Wavelength dispersion is in vertical direction with blue light on the bottom and red light on the top. One sub-region, a vertical stripe in the image, corresponds to a 2"x15" region in the datacube. This image equates to 3600 spaxels in the final datacube. There is visible distortion in the spectra. The green arrows point to the same emission lines from the arc lamp and the emission lines in the center of the image deviated from those on the sides. This is apparent when compared to the green horizontal line. This needs to be accounted for when reducing the datacube.

Flat field images are taken daily by the telescope operators. They are used to determine the variation in sensitivity between pixels in the CCDs. IFSs are uniformly illuminated by a continuum lamp, which has a known wavelength dependence with flux and a set of 11 exposures are taken for all IFSs. The exposures are used in recipe **muse_flat**, which combines the images by averaging. The recipe produces a master flat-field calibration image and a line trace file for every IFS. These traces are used to identify the location of every spectra i.e. spaxel on the CCD.

Next recipe to run is **muse_wavecal** and it is used to identify the location of a given wavelength on the CCDs. The calibration images contain emission lines from arc lamps including HgCd, Xe and Ne. The recipe identifies the emission line locations, cross-references these values to the pipeline's database and fits a polynomial as a dispersion function, describing wavelengths as a function of pixels.

muse_lsf generates line spread functions (LSF) for each slice in each of the IFSs, producing 30 LSFs at different wavelengths. It uses the same arc lamp exposures as **muse_wavecal**, as well as the line traces it produced. LSF effectively describes how the instrument itself spreads an infinitely narrow emission line. This is comparable to how a point spread function (PSF) describes the spatial spread of light from a point source.

There is now enough calibration data to extract data from the target and the standard star with the recipe **muse_scibasic**. As with twilight cube, raw exposures are reduced with the calibration files. Spectral lines are extracted and their locations on the FoV are identified. The extracted flux values are saved on a pixel table, a table containing all the necessary information to reconstruct the datacube, along with their three-dimensional coordinates; two spatial coordinates and one spectral coordinate. In the case of the standard star datacube the observed stellar flux is compared to the pipeline's standard star flux tables and the atmospheric extinction table using the recipe **muse_standard**. This allows for changing of the units from

the instrumental analog-to-digital units, a scalar describing the amount of exposure, to erg/s/cm^2/Å. The recipe also produces a model of the telluric absorption lines by comparing the known telluric absorption line regions in the spectra and the deviations between the observed and the standard flux table. Similarly an atmospheric emission line model is produced with recipe **muse_create_sky** from the empty sky parts of an exposure. These atmospheric models, the standard star response curve and the preceding pixel tables are finally used to produce the human-readable datacube with the recipe **muse_scipost**.

In the case that two or more exposures need to be stacked or mosaicked, the recipes **exp_align** and **exp_combine** can be used. Images of the FoVs of each of the exposures are required. A collapsed image of the full datacube or a strong emission line map can be used. The recipe **exp_align** identifies bright point-like sources in a given image and attempts to find matching source locations in other images. This creates a list of offsets for each datacube file that can then be passed to **exp_combine**. The recipe combines exposures together taking into account possible geometric distortions between them.

Three-dimensionality of the data allows different types of presentations for it. The full FoV of the final datacube is presented in Figure 2. Maps of isolated emission lines are presented in Figure 3.

4 Methods

In the proceeding methods, measurements, such as metallicity, are done separately for each spaxel in the FoV to produce results such as maps or pixel statistics. In addition, the SN locations are given special consideration. The SN locations are measured by integrating the flux coming from an area that corresponds to the PSF of the datacube. The measurements from these synthetic apertures are then used in comparison to the spaxels corresponding to the host galaxy. There are several

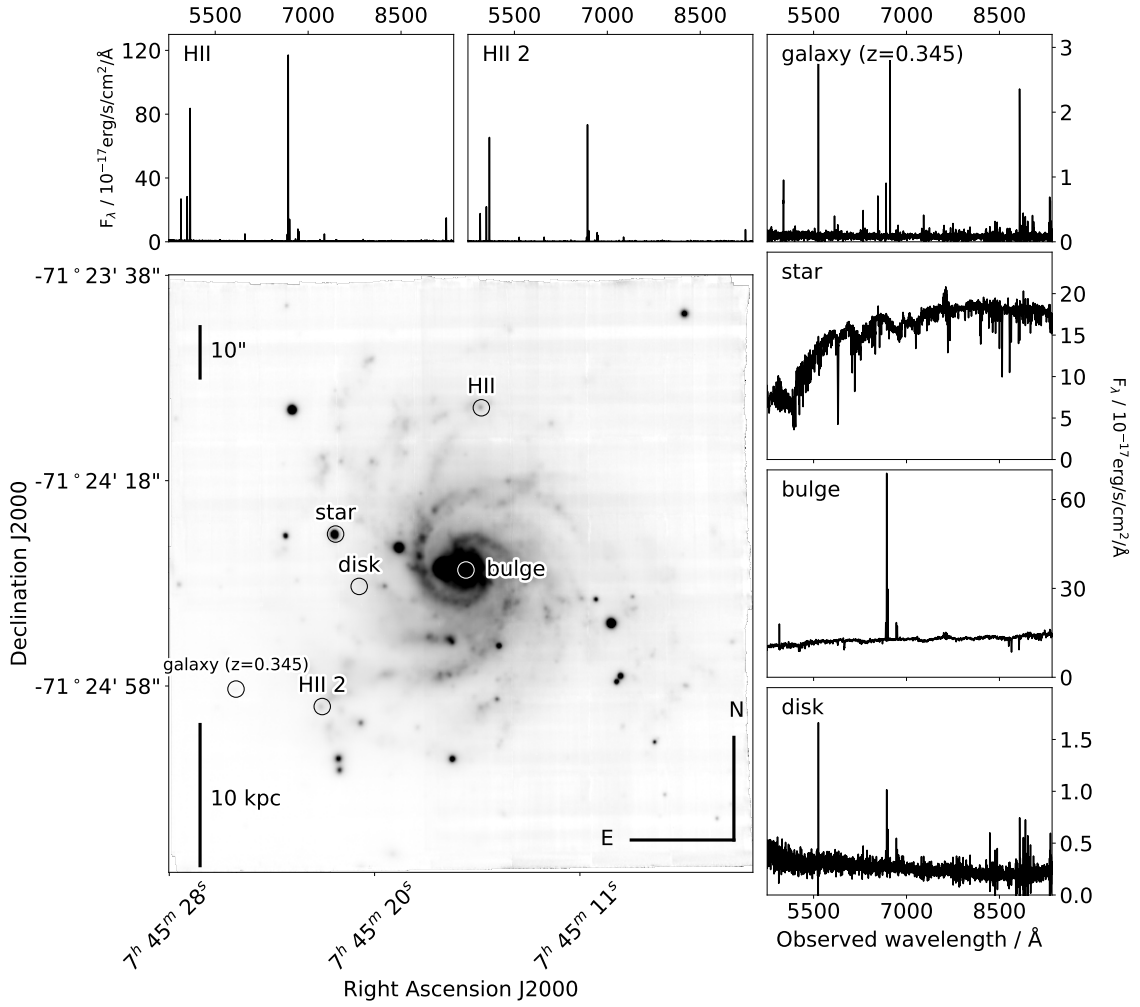

Figure 2. A collapsed datacube of the final mosaic with examples of extracted sample spectra. The mosaic FoV has dimensions of 2'x2'. The spectrum from each spaxel is summed up to produce a two-dimensional representation of the datacube. The field also contains objects unrelated to the host galaxy such as Milky Way stars in the foreground and a background galaxy. Most of the bright spots are foreground stars. Few stronger and brighter spiral arms are visible in the galaxy.

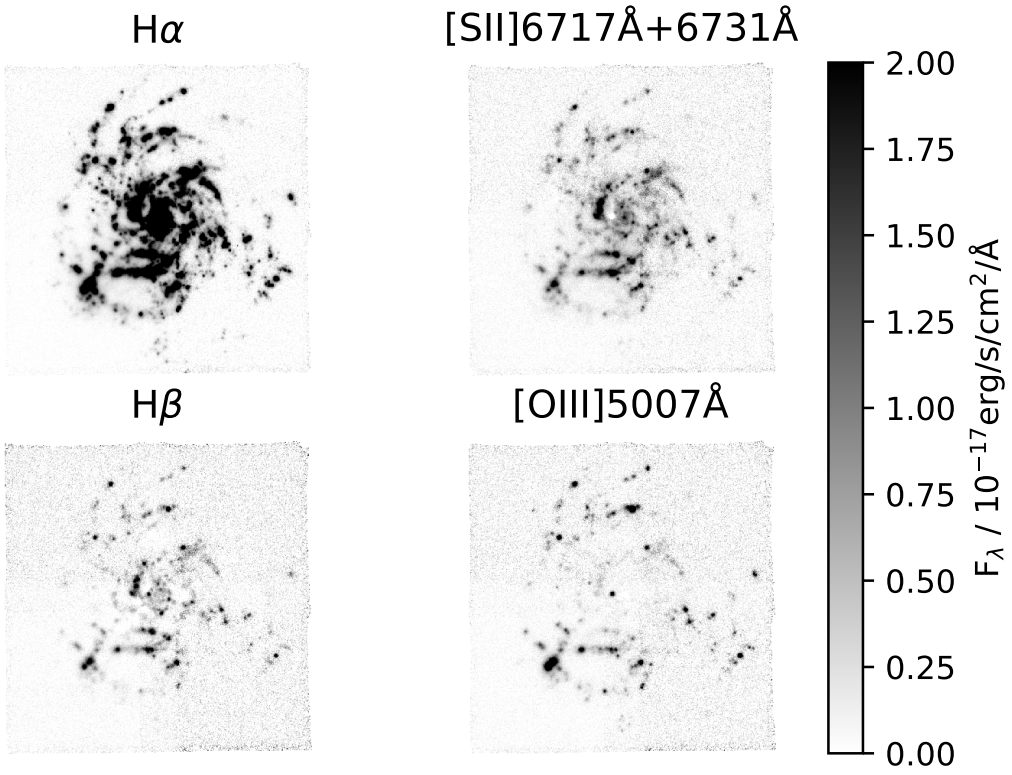

Figure 3. Several emission line maps extracted from the reduced datacube. [S II]$\lambda\lambda$6717,6731 has a slice width of 40 Å, the rest have a width of 20 Å. Continuum has been removed with a linear regression fit. Hα is clearly the brightest emission line in the galaxy and the flocculent structure is more visible here than in Figure 2. [O III]λ5007 emission from the galactic bulge is extremely weak and is mostly not detectable.

foreground stars surrounding the galaxy allowing a measurement of PSF. From the collapsed FoV of the datacube a FWHM for the foreground stars was measured to be about 0.7", except for the northeastern element containing ASASSN-14dd for which the FWHM was measured to be 1.0". For this reason the SN location spectra were extracted from the datacube with a synthetic circular aperture diameter of 0.8", except for ASASSN-14dd which was measured with an aperture diameter of 1.0".

4.1 Spectral continuum fitting

The continuum originating from the host galaxy is fitted with simple stellar population spectral energy distributions (SEDs) from the Binary population and Spectral Synthesis (BPASS)[42] using the program `STARLIGHT`[43]. In a simple stellar population model all the stars are assumed to be born at the same time from the same molecular cloud and there is no more star formation in the population. The stars also have the same metallicity as there is no metal enrichment happening during the formation period and the cloud is homogenous in metallicity. The BPASS version 2.1 is a simulation of a stellar population, which incorporates binary star systems. Binary interaction rejuvenate stars and makes the population seem younger than a purely single star population of the same age. This is especially pronounced in the first few tens of millions of years of a population because of the short lifetime of massive stars and the effect close companions have on them. Taking the effects of the binary populations into account is thus important for CCSN progenitor studies. In the simulation a population of stars with total initial mass of 10^6 $M_\odot$ is created at the beginning with a mass distribution according to some IMF. For this thesis the traditional Salpeter IMF with a mass range from 0.1 $M_\odot$ to 100 $M_\odot$ is adopted.[23] Binary systems in the simulation have three system parameters describing their initial conditions: initial orbital period from one day to 10,000 days, primary star

mass according to the IMF and secondary star mass as a fraction of the mass of the primary star with a range from 0.1 to 0.9. The orbital period might change during the evolution of the system due to, e.g., interaction between the extended stellar atmospheres which can also cause stellar mergers. These stars then evolve over time according to the stellar evolution models for several billions of years. The results from BPASS in addition to integrated SEDs at different epochs include SN rates and number of different stellar types present in the population. All results are available with metallicities from Z = 0.001 to Z = 0.040. Solar metal mass fraction adopted by BPASS is $Z_{\odot} = 0.02$. Solar oxygen abundance adopted in this thesis is $12+\log(O/H) = 8.66$.[44, 42]

STARLIGHT fits SEDs with different ages and metallicities from BPASS to a spectrum from the datacube. A mask file consisting of the most common emission lines is also given to the program to avoid fitting the lines instead of just the continuum. The fitting makes an initial assumption that the spectrum is composed of several stellar populations and tries to find the best combination to fit the observed spectrum. The program applies dust reddening in a given range to the SEDs to improve the fit. The lower limit for the range is the Milky Way extinction discussed in the next section and the upper limit is left open. Reddening is especially important in locations with young stellar populations as they are generally obscured by dust in star forming regions. STARLIGHT also produces best fits for single population models, producing χ^2 errors for the fit. This is an effective tool to verify the quality of the main fit. Continuum fitting is run through the whole datacube for every spaxel. These resulting continua are then removed from each spaxel to produce a continuum-subtracted datacube, that contains only the gas emission component of the galaxy. This method removes possible stellar absorption lines contaminating gas emission lines, producing more accurate measurements for the emission lines. The reduced datacube is then used for the proceeding line diagnostics.

Along with BPASS, Starburst99 (S99) SED data is also used for fitting SN location spectra.[45] S99 is a stellar population simulation that has been used extensively to study stellar populations although it neglects the existence of binary system. The S99 model is expected to produce age estimates that are younger than the BPASS estimates and will work here as a simple test to the BPASS results.

4.2 Interstellar extinction

Dust in the interstellar medium produces extinction to the light emanating from a source. The light from extragalactic sources suffer from two main sources of extinction: extinction originating from the dust in the Milky Way and the dust in the local source environment. Dust is especially efficient in absorbing shorter wavelength light which causes objects to appear redder than what they inherently are. This causes a problem with spectral fitting as a population's color changes as a function of time from blue to red. Without correcting for extinction the results would overestimate the ages.

Extinction is usually described by color excess,

$$E(B-V) = (B-V) - (B-V)_0, \tag{2}$$

where $(B-V)$ and $(B-V)_0$ are the observed and intrinsic color, respectively. Color excess corresponds to a total extinction in the V filter,

$$A_V = R_V \cdot E(B-V), \tag{3}$$

where an extinction curve parameter $R_V = 3.1$ is assumed for the Milky Way and a value $R_V = 4.05$ is assumed for the host galaxy.[46, 47] The host galaxy shows higher star formation activity than the Milky Way so a higher parameter value is justified. Using the extinction law of Cardelli et al. (1989) for standard interstellar extinction in our galaxy the spectrum is then dereddened. Milky Way color excess used in thesis in the direction of NGC 2466 is derived by Schlafly and Finkbeiner

(2011)[48], who used Sloan Digital Sky Survey (SDSS) data to recalibrate an earlier study by Schlegel et al. (1998)[49]. The color excess is estimated to be $E(B-V) = 0.141$ mag in the region of the host galaxy, corresponding to a visual extinction of $A_V \approx 0.44$ mag.

Observations have two major sources of extinction; the Milky Way and the host galaxy. The Milky Way lies in front of the host galaxy so it affects all observations. Extinction originating from the host galaxy is localized to different regions within the host galaxy and can be estimated from the spectra. Where possible, the host galaxy extinction is also removed from the spectra using the Balmer decrement, otherwise only the foreground extinction derived from the SDSS is removed. In interstellar medium the ratio of emission lines Hα and Hβ can be assumed to be a known constant. By measuring the observed line ratio, the color excess that causes the deviation from the theoretical value can be estimated,

$$E(B-V) = 1.97 \cdot \log_{10}\left(\frac{H\alpha/H\beta}{2.86}\right), \tag{4}$$

where 1.97 is an intrinsic parameter of Hα and Hβ describing the attenuation in these wavelengths in respect to the color excess assuming Calzetti et al. (2000) extinction law.[50] The value 2.86 is the so called case B theoretical flux ratio of Hα and Hβ assuming gas temperature T = 10^4 K and density n = 10^2 cm^{-3}.[51] The case B recombination assumes that no hydrogen ionising photons escape from the absorbing medium. The extinction map of the whole galaxy and the evaluated values for SN locations are presented.

4.3 Hα mapping

Hα flux is mapped throughout the datacube. The Hα emission originates from H II regions in the galaxy. These regions are defined as ionised regions of interstellar medium, where luminous short-lived OB spectral type stars produce photons with energies high enough to ionise hydrogen. Protons and electrons recombine and the

resulting excited hydrogen atoms emit the energy of the original photon as several new photons at longer wavelengths as the electron cascades down the energy levels. Hα emission can therefore be used for mapping of star-forming regions. The Hα emission line is extracted from the datacube and plotted as a map. The map is masked so that only spaxels with Hα signal-to-noise-ratio S/N > 3 are selected. An Hα map of the host galaxy is presented in Figure 3.

4.4 Pixel statistics

The host galaxy is studied through cumulative pixel value distribution function to compare the SN positions with the rest of the galaxy. For example, the pixels in the Hα map are sorted according to their pixel values from lowest to highest. The pixel with lowest flux is given a value of 0 and the pixel with the highest flux is given a value of 1. All pixels in between are given a value representing the number fraction of pixels that have a lower value than itself. These are then plotted on a graph where the y-axis shows the fraction of pixels below a given pixel value and x-axis the measured quantity. The SN locations are measured their characteristic values from the averaged flux of the PSF. This is done by adding up the flux inside the PSF at the SN location and dividing this value by the number of pixels inside the PSF. They are then plotted along the cumulative curve. Their position shows what kind of environments they are situated in. High cumulative fraction would, in the case of Hα pixels, indicate a bright H II region. This can be interpreted a location with a higher number of massive stars, which indicates a larger or younger star cluster.

Another related statistical method used is the normal distribution function. The pixel values are binned and plotted with the number of pixels in a bin as a function of the measured quantity. The measured values corresponding to SN locations are indicated in the plots. This alternative method is better at showing how homogenous

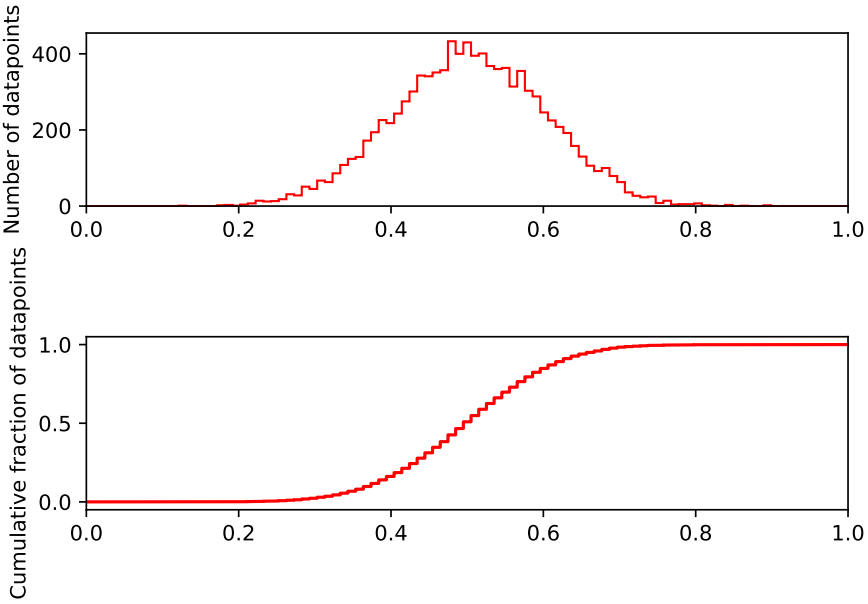

Figure 4. Examples of data samples used in pixel statistics. A set of random numbers are drawn from a normal distribution with σ=0.1 and μ=0.5. In the top figure the data are binned and plotted as the number of datapoints in respective bins, producing a distribution function. The same data are represented as a cumulative distribution function in the bottom figure.

the galaxy is and if the SNe prefer more uncommon pixel values deviating from the galaxy average. Examples of both methods are shown in Figure 4.

These methods are additionally used to study the relative metallicity and ionisation levels of the SN enviroments in respect to the rest of the galaxy.

4.5 Star formation and supernova rates from Hα luminosity

The Hα luminosity of a SN site can be used to estimate the star formation rate (SFR) in that region. The SFR can be calculated from the formula

$$\mathrm{SFR}(\mathrm{M}_\odot \mathrm{yr}^{-1}) = 7.9 \cdot 10^{-42} \mathrm{L}(H\alpha)(\mathrm{erg\ s}^{-1}), [52] \tag{5}$$

where the Hα luminosity L($H\alpha$) is calculated from Hα flux F(Hα), in units of erg/s/cm^2 and the luminosity distance d_L, in units of cm,

$$\mathrm{L}(H\alpha) = 4\pi d_L^2 F(H\alpha). \tag{6}$$

Only the most massive OB-type stars produce considerable amounts of ionising radiation to the gas that produces the Hα luminosity in the ISM. These stars are short-lived so the measurement yields the SFR of only the most recent 20 Myr. CCSNe are all produced by short-lived massive stars, so it is assumed that these SNe are born within a region with a higher SFR or at least in a proximity to one. This is in contrast against the thermonuclear type Ia SNe, which are produced by stars with ages from hundreds of millions to billions of years.[53] These SNe should not show a preference to the SFR of the surrounding region. The SFR value is directly linked to the CCSN supernova rate (SNR) of the region. Adopting the initial mass function from Salpeter (1955)[23] and assuming that stars with initial masses of over 8 $M_\odot$ or larger will always produce a CCSN, the fraction of mass going into SN progenitors is (assuming a possible stellar mass range from 0.1 $M_\odot$ to 30 $M_\odot$),

$$f_{SN} = \frac{\int_8^{30} M \cdot M^{-2.35} dM}{\int_{0.1}^{30} M \cdot M^{-2.35} dM} = 0.0925 \tag{7}$$

and the average mass of a CCSN progenitor is

$$\langle M \rangle = \frac{\int_8^{30} M \cdot M^{-2.35} dM}{\int_8^{30} M^{-2.35} dM} = 13.73 \ M_\odot. \tag{8}$$

Alternatively, if the maximum stellar mass is assumed to be 100 $M_\odot$. The mass fraction then rises to $f_{SN} = 0.139$ and the average mass for a CCSN progenitor $\langle M \rangle$=18.73 $M_\odot$. SNR can be calculated from the SFR as

$$\mathrm{SNR}(\mathrm{yr}^{-1}) = \frac{f_{SN}}{\langle M \rangle} \mathrm{SFR}. \tag{9}$$

4.6 Equivalent width mapping

Another constraint for stellar population ages can be obtained by comparing the observed equivalent width (EW) to the values produced by simulations. EW of an emission or absorption line is defined to be the width of the rectangular area under the continuum that has the same total flux as the line profile (Figure 5).

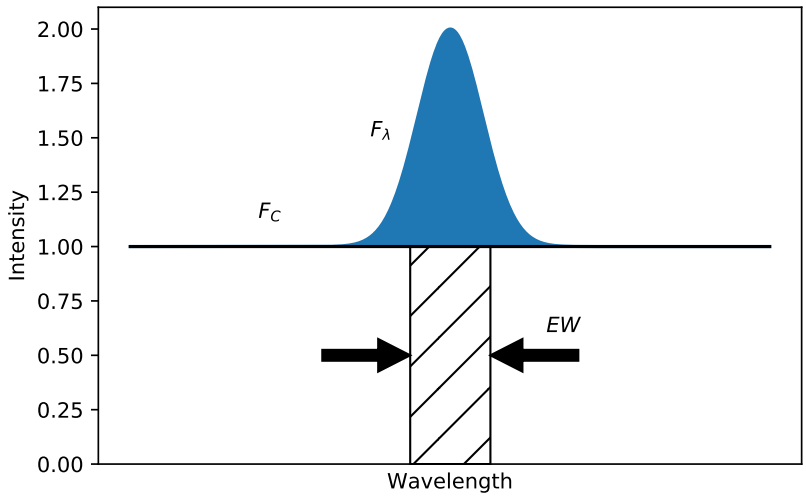

Figure 5. Schematic view of EW in arbitrary units. The area of emission line flux, colored blue, is equivalent to the area below continuum flux (diagonal hatch). EW is the width of the hatched area in wavelength units. Here the continuum is flat and normalized, but usually the shape of the continuum needs to be taken into consideration by normalising it to unity.

Numerically this is defined as the total flux coming from the emission line divided with the continuum flux at that wavelength,

$$EW = \frac{F_\lambda - F_C}{F_C} d\lambda, \tag{10}$$

where F_C and F_λ are the continuum flux and line flux, respectively.

ISM in galaxies shows several emission lines that can be used to interpret the age of the surrounding stellar population. BPASS SEDs have been used to simulate the ISM emission lines as a function of time.[54] Additionally, a version of BPASS including only single stars populations and S99 emission line data are used produce similar emission line evolution data.

Nebular data are available for wide range of metallicities, ionisation parameters and densities of ISM. The relationship between EW and age vary slightly due to these parameters, so models closest to the observed values are used. The ISM density is assumed to be 100 cm^{-3}. The EW decreases nonlinearly over the age of the stellar

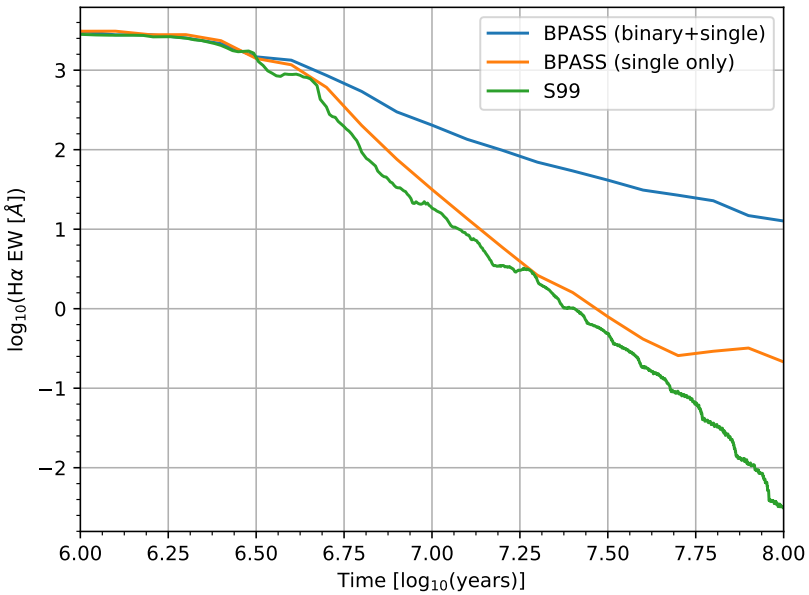

Figure 6. Comparison of Hα EW from different models as a function of the age of the stellar population. In the models all stars are born instantaneously and the time axis is years after formation. Metallicity in each model is Z=0.008. The effects of binary systems to the EW are notable after about 5 Myrs.

population, especially during the disappearance of massive WR stars at roughly 5 Myrs. For this reason I will only consider the first age interval that has the same EW as the minimum age of the population. The evolution of EW in different models is presented in Figure 6.

4.7 Ionisation parameter

The ionisation parameter measures the ratio of the neutral and ionised hydrogen in the ISM,

$$\mathrm{U} = \frac{\mathrm{n}_\gamma}{\mathrm{n}_H} \tag{11}$$

where n_γ and n_H are the number density of ionising photons and hydrogen atoms, respectively.[55] An ionising photon is defined as any photon that has energy high enough to ionise a hydrogen atom from the ground state, $\epsilon \geq$13.6 eV. Higher value of

U implies higher number density of ionisizing photons and thus presence of younger, blue stars. Typically, a young H II region has values of $\log_{10}$U > -3.0. The ionisation parameter is studied using two similar methods. Diaz et al. (1991)[56] shows that the ratio of the forbidden lines [S II]$\lambda\lambda$6717,6731 and [S III]$\lambda\lambda$9069,9532 is an effective tool to measure the ionisation parameter

$$\text{logU} = -(1.684 \pm 0.076) \cdot \log\left(\frac{F([S\ II])}{F([S\ III])}\right) - (2.986 \pm 0.027), \tag{12}$$

where F([S II]) and F([S III]) are the fluxes of the emission lines. Only one of the [S III] emission lines are within the MUSE wavelength range, so a theoretical line ratio of [S III]λ9532 = 2.44·[S III]λ9069 from [57] is used to correct for this. Additionally, Dors et al. (2011)[58] have produced an alternative method to estimate the parameter,

$$\text{logU} = -(1.66 \pm 0.06)\log\left(\frac{F([S\ II])}{F(H\alpha)}\right) - (4.13 \pm 0.07), \tag{13}$$

which is independent of metallicity when metallicity is higher than one fifth of solar.

4.8 Photometry

The MUSE datacube has a large wavelength coverage, so it is also possible to produce broad band images from it for photometry. This is done by integrating over the wavelength a part of the cube that corresponds to that filter. The wavelength-dependent filter response function is also taken into account to provide an accurate modeling of a filter. This method is provided with the reduction pipeline as recipe **muse_cube_filter.** Three filters have been selected for photometry: Johnson V, SDSS r and i filter. These three filters are fully covered in the datacube and can then be effective tools for photometry. The brightness of the SN region is measured in each filter.

4.9 Metallicity mapping

Emission lines are used to estimate the metallicity of the gas. Relative line strengths of a given element to hydrogen can imply higher abundance, but the electron density and temperature of the gas also play an important role in line strengths. Oxygen is the traditional tracer for metallicity because the optical forbidden emission lines are relatively strong. Oxygen is also the most abundant metal in the universe making the lines easier to detect. They can also be used as probes of electron density and temperature by themselves.[59] In this work N2 and O3N2 indices from Marino et al. (2013)[60] and S2 index from Dopita et al. 2016 [61] are used to estimate the oxygen abundance in the host galaxy and at the SN locations. They use strong emission lines from different elements, which are compared to the strength of hydrogen lines, to measure the ratio of oxygen to hydrogen in the ISM. N2 method uses the ratio of two adjacent emission lines Hα and [N II]λ6584,

$$\log(\mathrm{O/H}) + 12 = 8.743 + 0.462 \cdot \log\left(\frac{F([N\ II)]}{F(H\alpha)}\right), \tag{14}$$

and O3N2 uses additional lines of Hβ and [O III]λ5007

$$\log(\mathrm{O/H}) + 12 = 8.533 - 0.214 \cdot \log\left(\frac{F([O\ III]/F(H\beta)}{F([N\ II])/F(H\alpha)}\right). \tag{15}$$

S2 is similar to N2, but also implements the sum of two forbidden sulphur lines [S II]$\lambda\lambda$6717,6731

$$\log(\mathrm{O/H}) + 12 = 8.77 + \log\left(\frac{F([N\ II])}{F([S\ II]}\right) + 0.264 \cdot \log\left(\frac{F([NII])}{F(H\alpha)}\right). \tag{16}$$

The number of WR stars in a given population correlates with metallicity, as a higher metal fraction allows a lower initial mass for a WR star. More massive stars are monotonically rarer than less massive stars as implied by all of the IMFs. By increasing the metallicity of a population, the threshold mass for a WR star is lowered. This is due to stellar winds and mass loss rate increasing with metallicity, due to metals increasing the momentum transfer from light to atoms, making it

easier for a star to evolve into a WR star. For this reason increasing metallicity increases the number of WR stars in a given stellar population. This implies that SNe with WR progenitors would be more likely found in high metallicity regions.

4.10 Velocity mapping

Galaxy rotation velocity generally increases as a function of distance from the nucleus. In interacting galaxies there might be localized azimuthal or radial deviations and a velocity map can reveal evidence of a recent galaxy interaction. SN locations can also show radial migration that can affect the metallicity estimates. Recently, some evidence of azimuthal velocity variation around spiral arms has been found, indicating radial migration in these areas.[32]

Line-of-sight velocity map is produced from the blue- and redshifted Hα emission lines, in respect to the galaxy nucleus, on the galaxy disk. The emission line is fitted with a gaussian profile which has a center point at wavelength λ_e. This is compared to the rest wavelength at the galaxy nucleus and the velocity is calculated from

$$v = c\frac{\lambda_e - \lambda_n}{\lambda_n}, \tag{17}$$

where λ_n is the wavelength of Hα in the galaxy nucleus and c is the speed of light. In this way the recessional velocity of the galaxy due to the expansion of the Universe is removed and what is left is the observed velocity component of the gas.

5 Results and discussion

The host galaxy is more active in star formation than an average galaxy by a factor of few with a total star formation rate of 5.1 $M_\odot$/yr. For comparison Andromeda galaxy has a measured SFR of about 0.4 $M_\odot$/yr and Milky Way has an estimated SFR around one $M_\odot$/yr.[62, 63] This could indicate that the galaxy is interacting with another galaxy (Table 1). NGC 2466 has two visually close neighbouring galaxies.

2MASS J07443863-7122278 is an elliptical galaxy with a separation of 220", or 80 kpc, to NGC 2466 at the measured redshift. Difference in the radial distance to the two galaxies is small, under a megaparsec, assuming that observed recession velocity difference is not due to peculiar velocity. A spiral galaxy 2MASS J07461002-7122406 is also visually near NGC 2466 with a distance of 284" or 103kpc (Figure 7). This galaxy also has a recent supernova, MASTER OT J074610.09-712224.9, a type Ia SN first detected in April 26th 2015. It is possible that these galaxies are part of a local group and are interacting. NGC 2466 shows no anomalous velocities in the disk which would indicate disturbation through interaction (Figure 8). The galaxy SFR has been previously estimated by Sánchez-Menguiano et al. (2018)[38], finding a value three times higher. They measured the SFR using Hα luminosity, but used only H II region emissions and decoupled the continuum emissions using different SSPs. Different extinction estimations could also affect the measurements especially in the more nuclear parts of the disk. Extinction map of the galaxy is presented in Figure 8. They also calculated galactic metallicity gradient using the O3N2 tool, finding similar results, but with a slightly deeper slope. Metallicity gradients measured in this thesis are presented in Figure 9. The differences in measurements could be due to the other study's dependence on H II regions and the bias produced in them, as seen in Figure 10. The S2 tool used in Figure 11 shows no bias for H II regions.

Supernova rate for CCSNe indicates an average of one supernova event every 30 years in the galaxy. The observed three transients between years 2014 and 2016 is high compared to this, but not out of ordinary. The bulge area has moderate extinction due to dust (Figure 8). Considering that the distance modulus for NGC2466 from the measured redshift is m-M=34.42 mag, taking into account the Milky Way extinction and assuming that SN sky survey limiting magnitude with V filter is 17 mag, required absolute magnitude for a SN is M_V<-17.86 mag. Adding a possible

Coordinates		SFR	$SNR_{30M_\odot}$	$SNR_{100M_\odot}$	Redshift
RA	Dec	$M_\odot yr^{-1}$	yr^{-1}	yr^{-1}	z
07:45:15.963	-71:24:37.63	5.1	0.034	0.037	0.0178

Table 1. Host galaxy measurements. Star formation and supernova rates are integrated over the whole galaxy. Supernova rates are calculated assuming maximum stellar mass of 30 $M_\odot$ and 100 $M_\odot$.

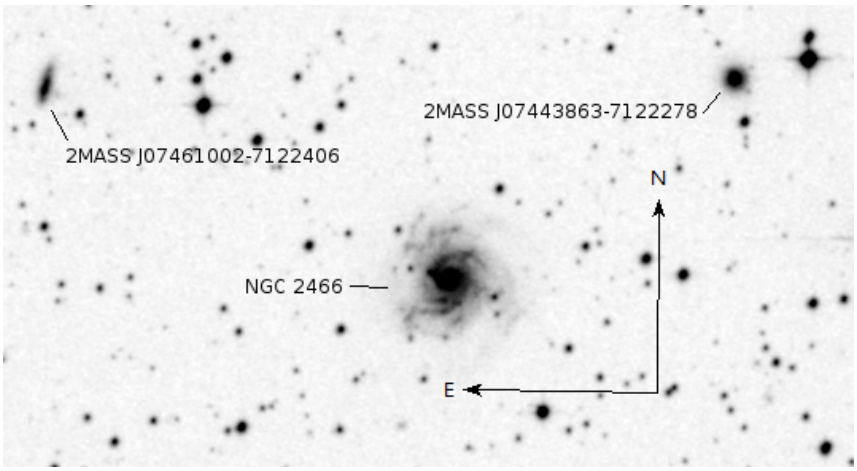

Figure 7. Field surrounding NGC 2466 from Digitized Sky Survey 2.

local dust shrouding to this, it is possible that some of the fainter SN types such as IIP and IIb are simply not observed.[64, 65]

The host galaxy contains six separate regions with considerably high Hα EW values, over 500 Å (Figure 12). These values indicate star formation regions with ages under 7 Myr and are most likely WR regions. The so-called blue and red bump associated with WR stars, broad HeII 4686 Å and CIV 5808 Å emission lines as described by Kehrig et al. (2013)[66], are not visible in these regions. Additionally HeI emission line at 4922 Å, which disappears from the population spectrum after 6 Myr, is not observed in the host galaxy. Integrating the whole galaxy spectra together yields no recognizable features. These lines are relatively weak compared to the S/N of the continuum, so their absence does not mean the absence of these stars, just that they cannot be observed directly in the spectrum.

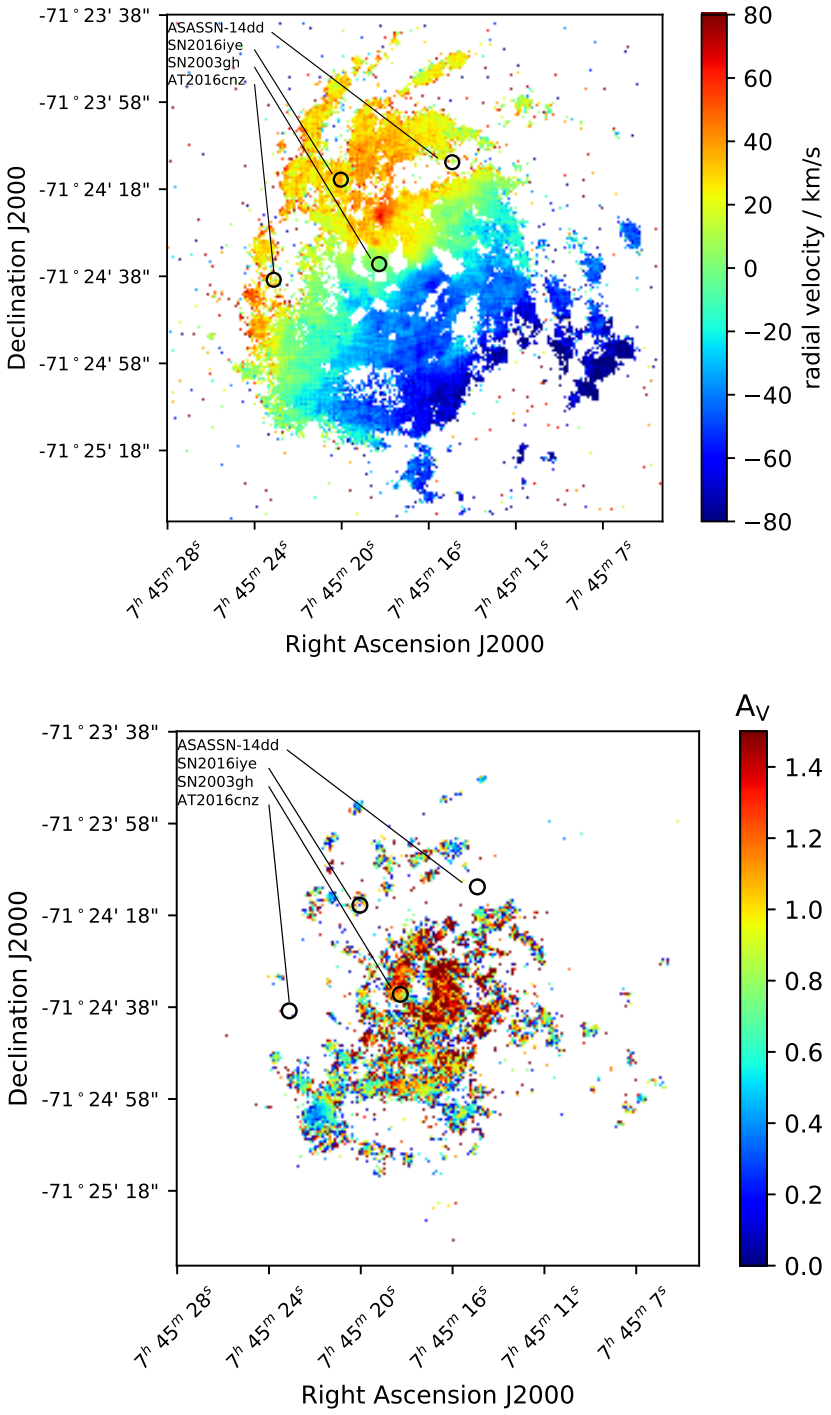

Figure 8. Velocity map of the galaxy (top) derived from the Hα emission line shifting in wavelength when compared to the central wavelength for the line at the position of the nucleus. Extinction map of the galaxy (bottom) as calculated from the Balmer decrement. Central bulge area is the most dusty region and extinction decreases with radius. Wherever Hα and Hβ can be identified, extinction is larger than the estimated Milky Way extinction $A_V \approx 0.4$.

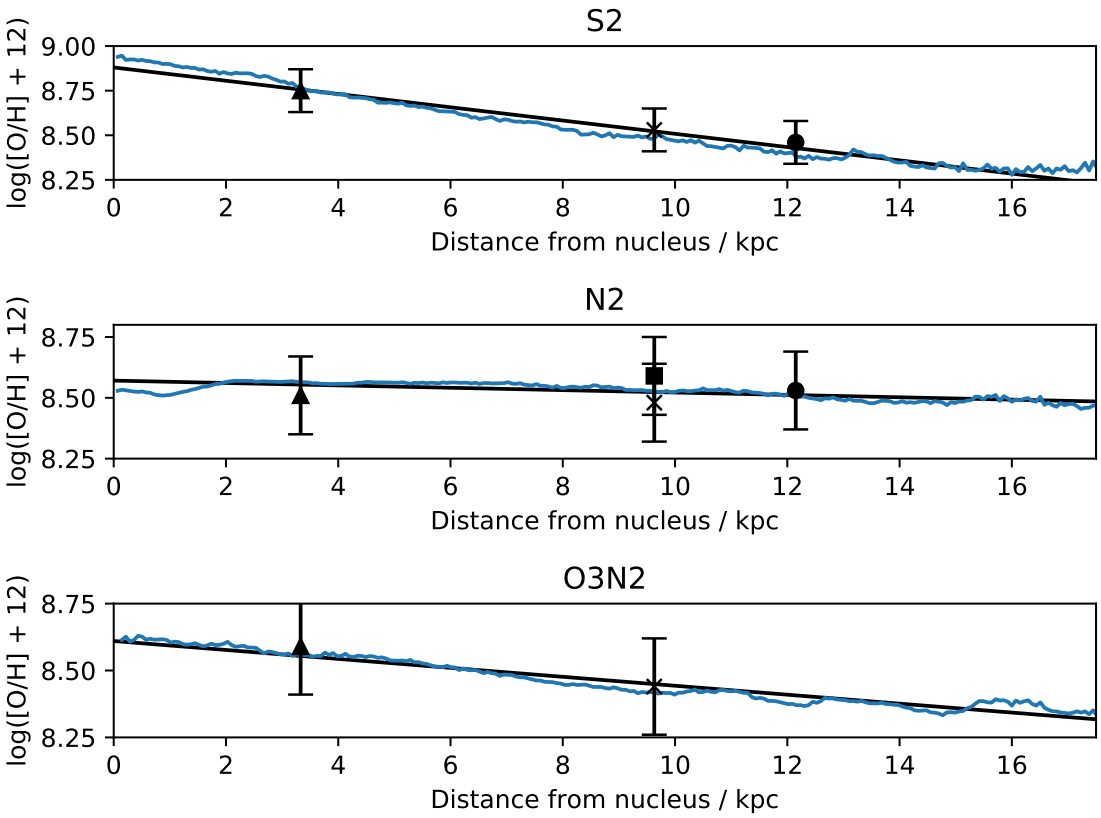

Figure 9. Metallicity of the galaxy as a function of distance from the nucleus. Blue line represents mean metallicity measurements as concentric rings around the nucleus in each metallicity index. Black line represents a linear least squares fit of the metallicity gradients. SNe ASASSN-14dd (square), AT 2016cnz (circle), SN 2016iye (cross) and SN 2003gh (triangle) are plotted at their radial locations in the host galaxy. The metallicity gradients are -0.037 dex/kpc, -0.005 dex/kpc and -0.017 dex/kpc, respectively for each index.

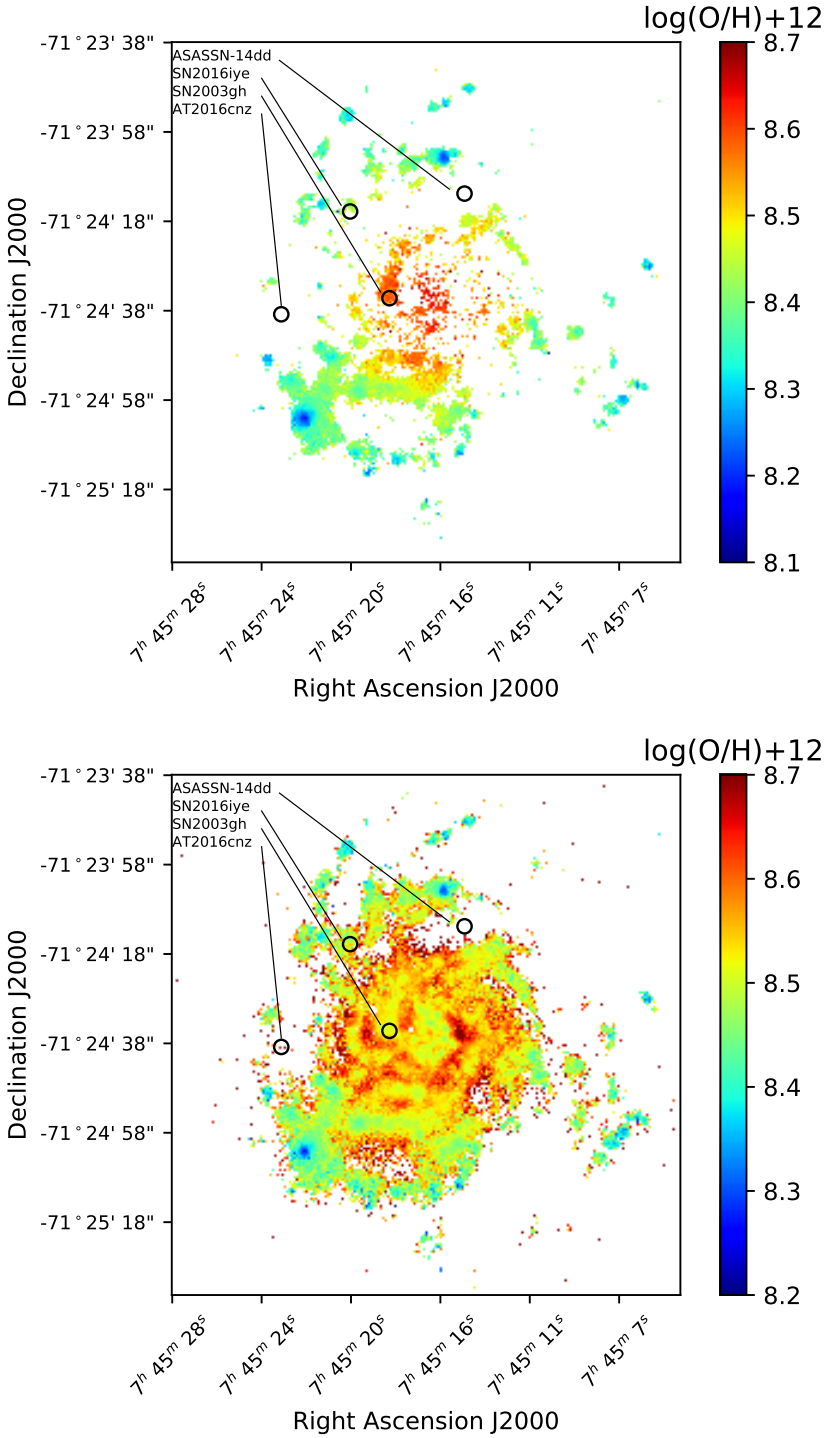

Figure 10. O3N2 (top) and N2 (bottom) metallicity maps of the galaxy. The number density ratio of oxygen atoms to hydrogen in the ISM is presented logarithmically over the whole galaxy where the emission lines are strong enough for reliable measurement. Emission lines Hα, Hβ, [O III]λ5007 and [N II]λ6584 are used. The non-detection of [O III]λ5007 in the galaxy core, as seen in Figure 3, makes the measurements using this line not possible in that area.

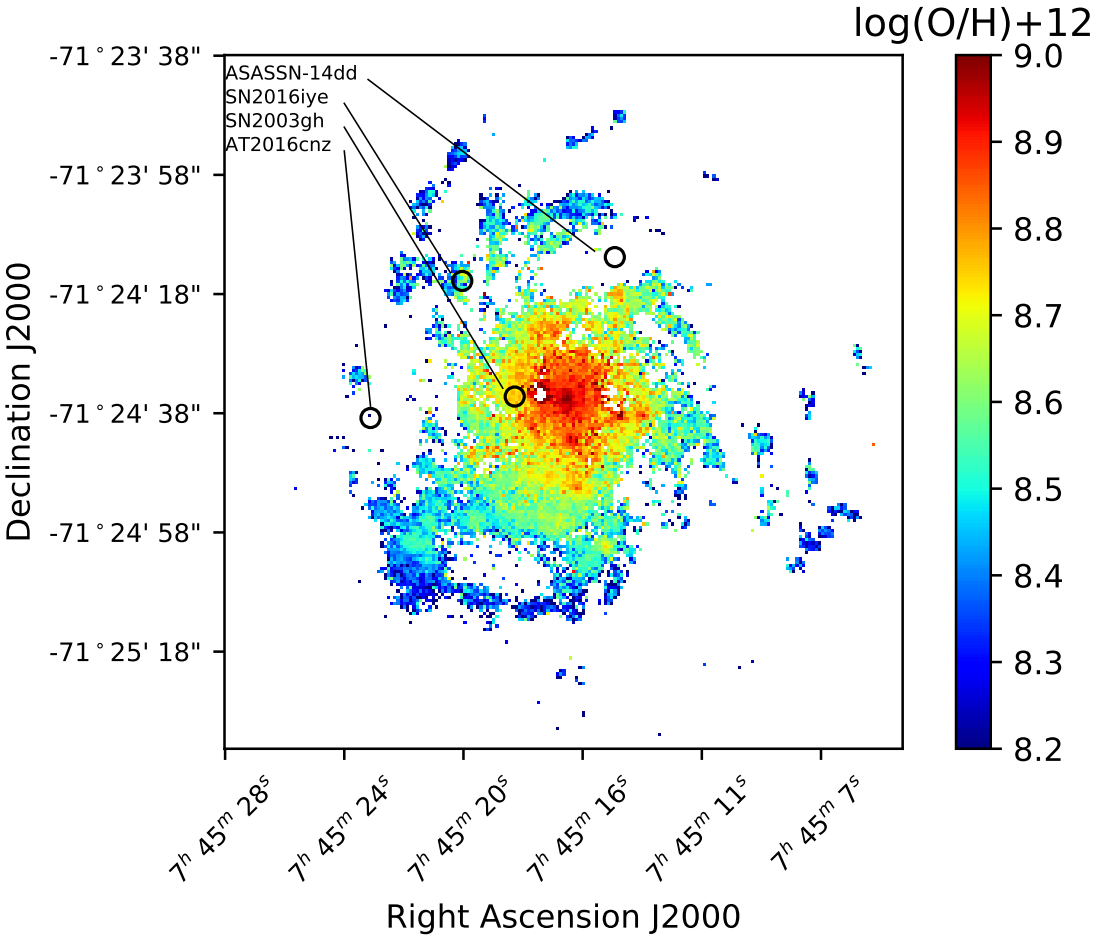

Figure 11. S2 metallicity map of the galaxy. The number density ratio of oxygen atoms to hydrogen in the ISM is presented logarithmically over the whole galaxy where the emission lines are strong enough for reliable measurement. Emission lines of Hα, [N II]λ6584 and [N II]$\lambda\lambda$6717,6731 are used.

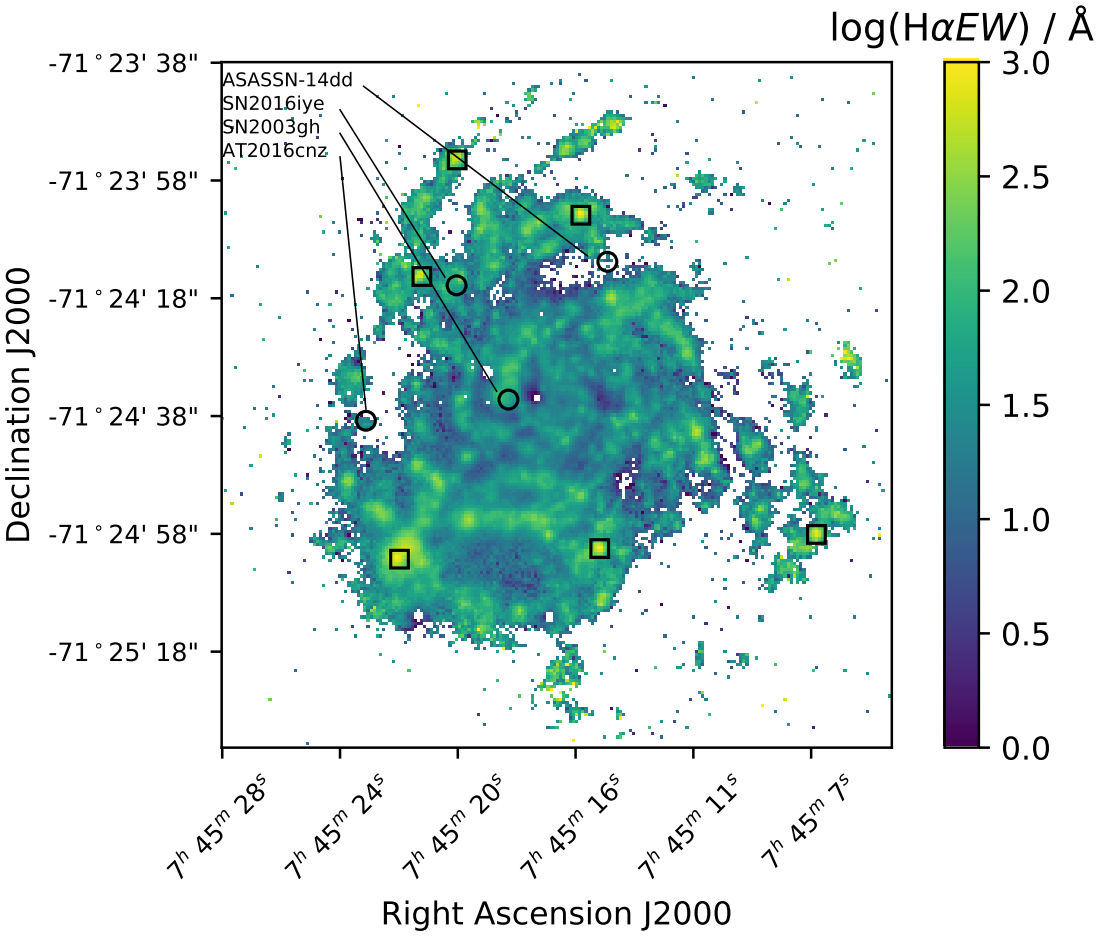

Figure 12. Equivalent width map of Hα on a logarithmic scale. Higher values indicate higher Hα luminosity compared to continuum, which is a sign of more recent star formation. Six regions (black squares) have unusually high equivalent widths of over 500 Å and up to 1200 Å.

Figure 13 show the statistical distribution of ionisation parameter pixels. Pixels with values higher than -3.0 are rare, only a few percent of the measured pixels. These are mainly concentrated in the galactic bulge and few star forming regions near the outer rim of the host galaxy, visible in Figure 12. Figure 14 shows ionisation maps created by two different methods. The method that uses only sulphur emission lines shows higher variation in the ionisation parameter, but also suffers from a higher systematic noise in MUSE's red end of the spectrum. None of the SNe locations are nearby these highly ionised regions undergoing star formation.

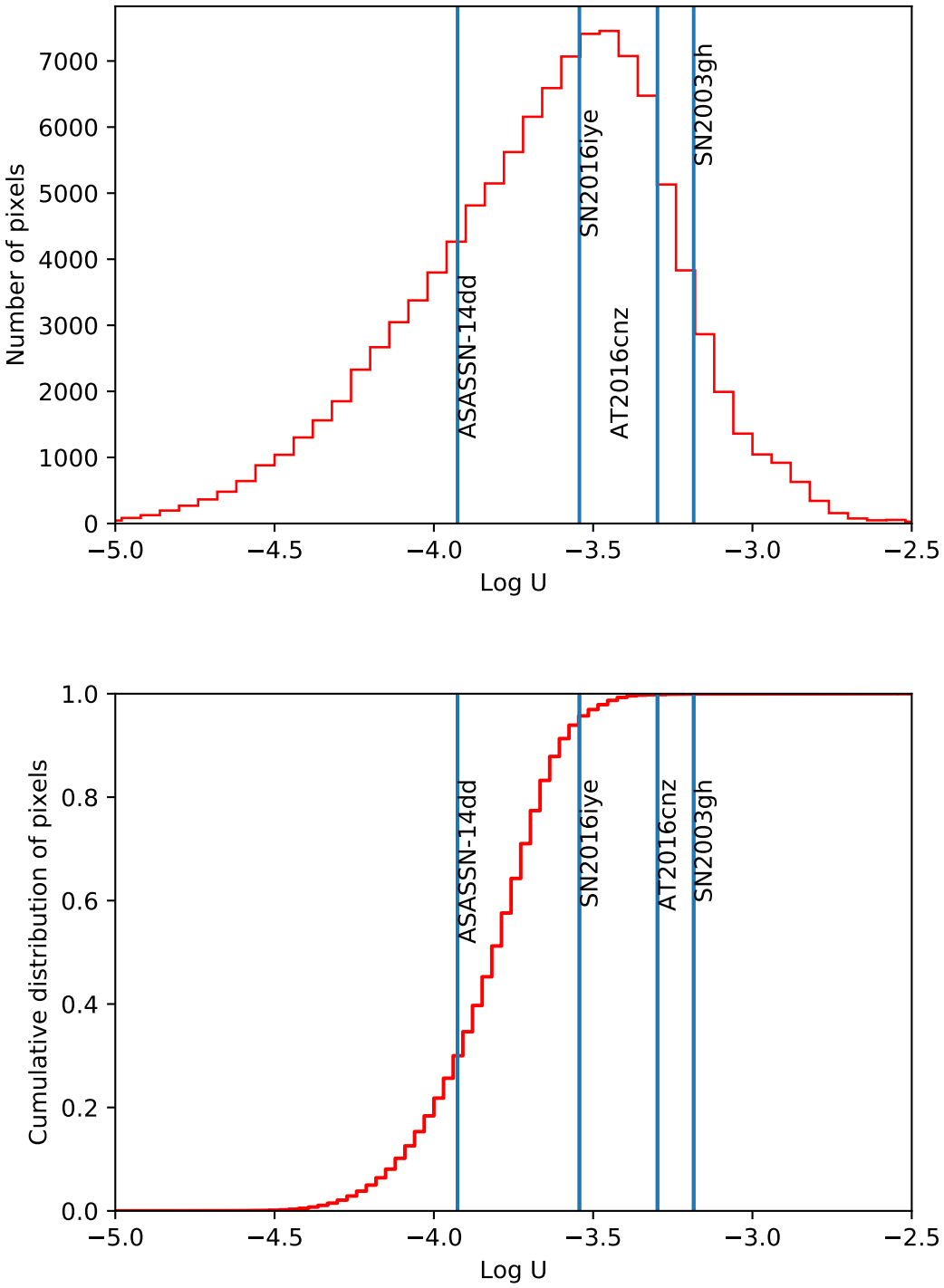

Figure 13. Distribution function and cumulative distribution of ionisation parameter pixels using the ratios of [S II]$\lambda\lambda$6717,6731 and Hα.

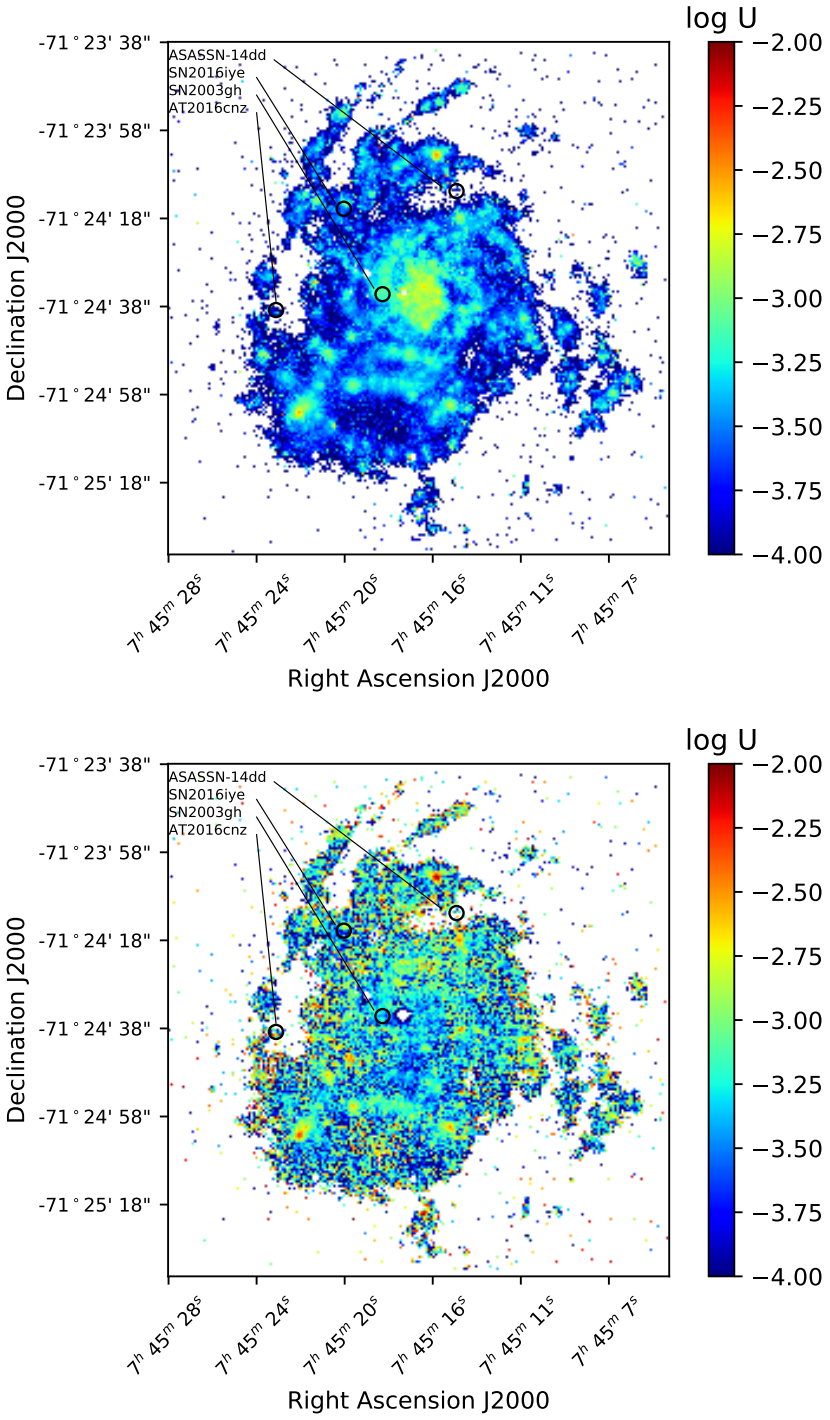

Figure 14. Ionisation parameter maps of the galaxy using the ratios of [S II]$\lambda\lambda$6717,6731 and Hα (top), and the ratios of [S II]$\lambda\lambda$6717,6731 and [S III]$\lambda\lambda$9069,9532 (bottom)

5.1 Difference between metallicity measurements

With MUSE's spatial resolution it is apparent that the degree of ionisation in the ISM affects the measured metallicities as previously suggested by Krühler et al. (2017)[67]. When maps in Figure 14 are compared to the metallicity maps in Figure 10, areas with higher degree of ionisation show lower metallicities in both methods. This also correlates with brighter and more recent star forming regions seen in Figure 12. Figure 11 uses the newer S2 method instead and seems to be more invariant to ionisation. Both O3N2 and S2 clearly exhibit the radial dependence of metallicity, which is also visible in Table 9. N2 has a flatter metallicity gradient, caused by the strong variability between spaxels with different ionisation parameters at same distances (Figure 9).

These results propose that, at distances where H II regions can be clearly discerned from the surrounding ISM, S2 method should be preferred. This corroborates the findings in Krühler et al. (2017).

5.2 Supernova enviroments

Resolution of the observations are high enough to observe the immeadiate area of few hundred parsecs of the SNe. Only one of the transients in the galaxy, SN 2016iye, are located within a PSF of H II region that is highly luminous in Hα band (Figure 15). ASASSN-14dd and AT 2016cnz are in smaller H II regions that have detectable line emissions, SN 2003gh is in within one of main spiral arm structures close to the bulge. The Hα EW age of these locations, derived from Starburst99 data, all produce ages that are under 10 Myrs (Tables 2 and 3). Because the S99 model does not include binary systems, these ages are should be taken as lower bounds of the region. Binary interaction within the population causes the population to appear younger than what solitary star populations would indicate. Zapartas et al. (2017)[53] show that certain types of CCSNe can be delayed as much as 200 Myr

with the aid of binary interactions. Indeed when BPASS population models are compared to the SNe environments, they produce ages that are older than the S99 model with ages ranging in few tens Myrs. Best fits of BPASS population models to observed SNe locations are presented in Figures 18 and 19.

5.3 ASASSN-14dd

This type Ibn SN was discovered in June 24 2014 with an apparent magnitude of m_V=15.6 mag. It was subsequently classified as type Ibn on July 6 matching to SN2006jc with a phase of 6 days after maximum light. This would make the first detection before maximum with an absolute magnitude of M_V=-19.3 mag. No follow-up observations have been published in literature.

The fraction of Hα flux inside the SN galactocentric radius is 0.7, as shown in Figure 16. In a previous study[68] the average fraction for Ib SNe was found to be 0.406. 16 of 22 type Ib SNe in the study detected nearer to the nucleus than ASASSN-14dd. This can be understood as an indication that Ib SNe prefer high metallicity inner parts of the host galaxy and ASASSN-14dd could more likely be from a low metallicity environment. The SN location is also in a relatively dim area of the disk, between two spiral arms, as evidenced in Figure 15. Figure 17 also show that the location is statistically in the main body of the disk, the dimmer inter-arm region.

Only the N2 tool could be used to measure metallicity in the region, because the required [O III]λ5007 and [S II]$\lambda\lambda$6717,6731 lines could not be detected (Table 2). 12+log(O/H) of 8.59 is relatively close to solar metallicity of $12+\log(O/H)_\odot$=8.66[44], but still slightly lower. In pixel statistics the SN region seems to be a higher than average in metallicity (Figure 20). This is likely to be an artifact from the bias in the method, as discussed before.

The inferred age of the region from BPASS SED fitting is over 30 Myr. This

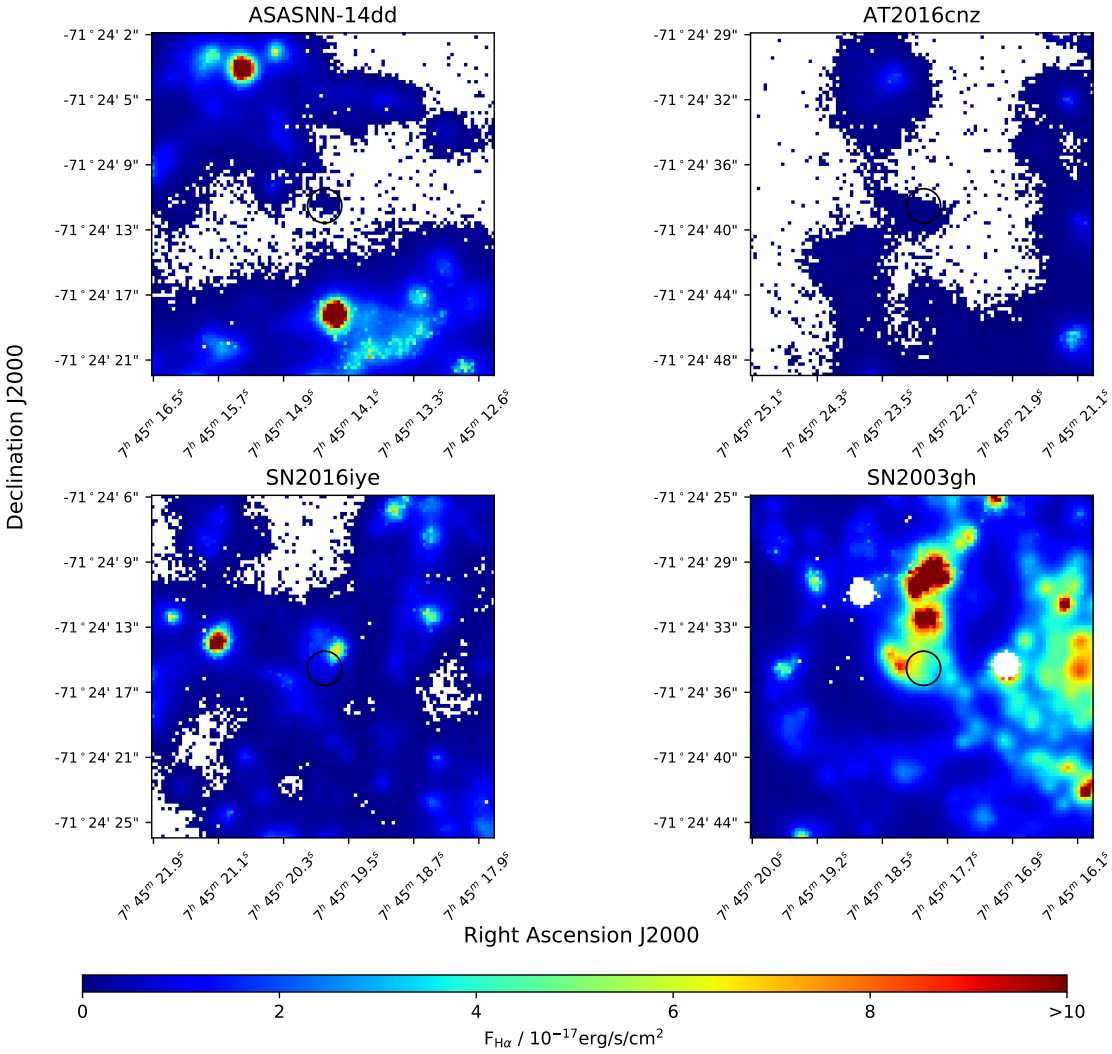

Figure 15. Closeups of the supernova locations in the galaxy reperesented with a Hα emission map. Black circles show the location of the SN and the PSF at that location. Faintest visible spaxels have luminosities of $3 \cdot 10^{35}$ erg/s and faintest identifiable structures have luminosities of $3 \cdot 10^{37}$erg/s. These structures are brighter than the Orion Nebula by a factor of few. All of the SNe are within detected Hα emission regions. ASASSN-14dd, a type Ibn SN, is in a noticeably small and solitary region between two larger spiral arm structures. The unclassified transient AT 2016cnz is within a tenuous arm. SN 2016iye, a type IIb SN, is next to a compact bright region. SN 2003gh, a type Ia SN, is embedded in one of the strong and bright spiral arms near to bulge, a bright mass to the east of the SN.

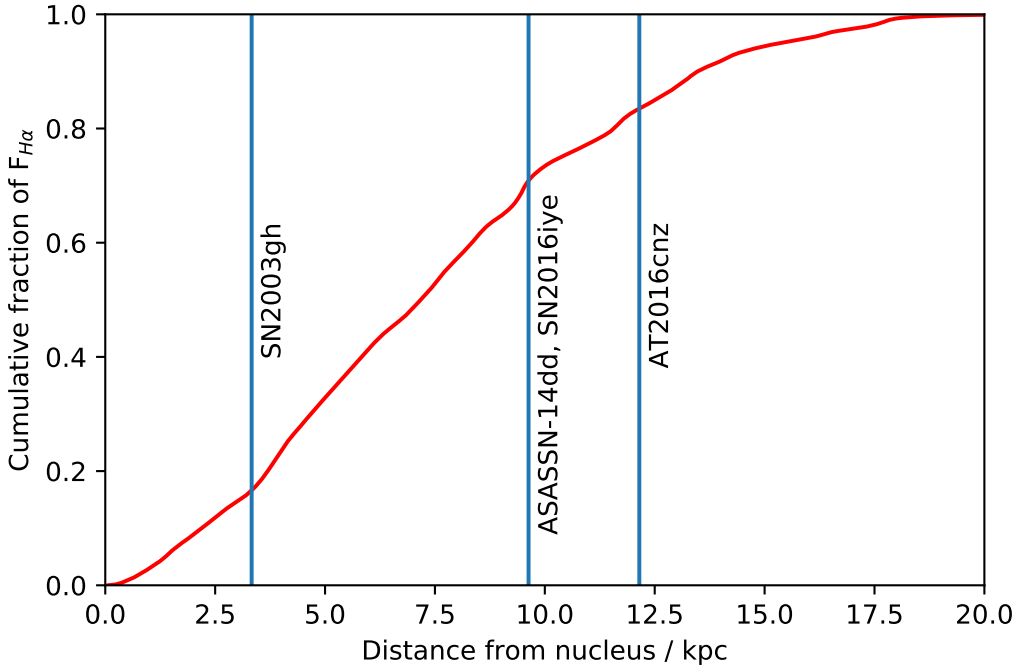

Figure 16. Cumulative distribution of Hα flux as a function of radius from the galaxy nucleus.

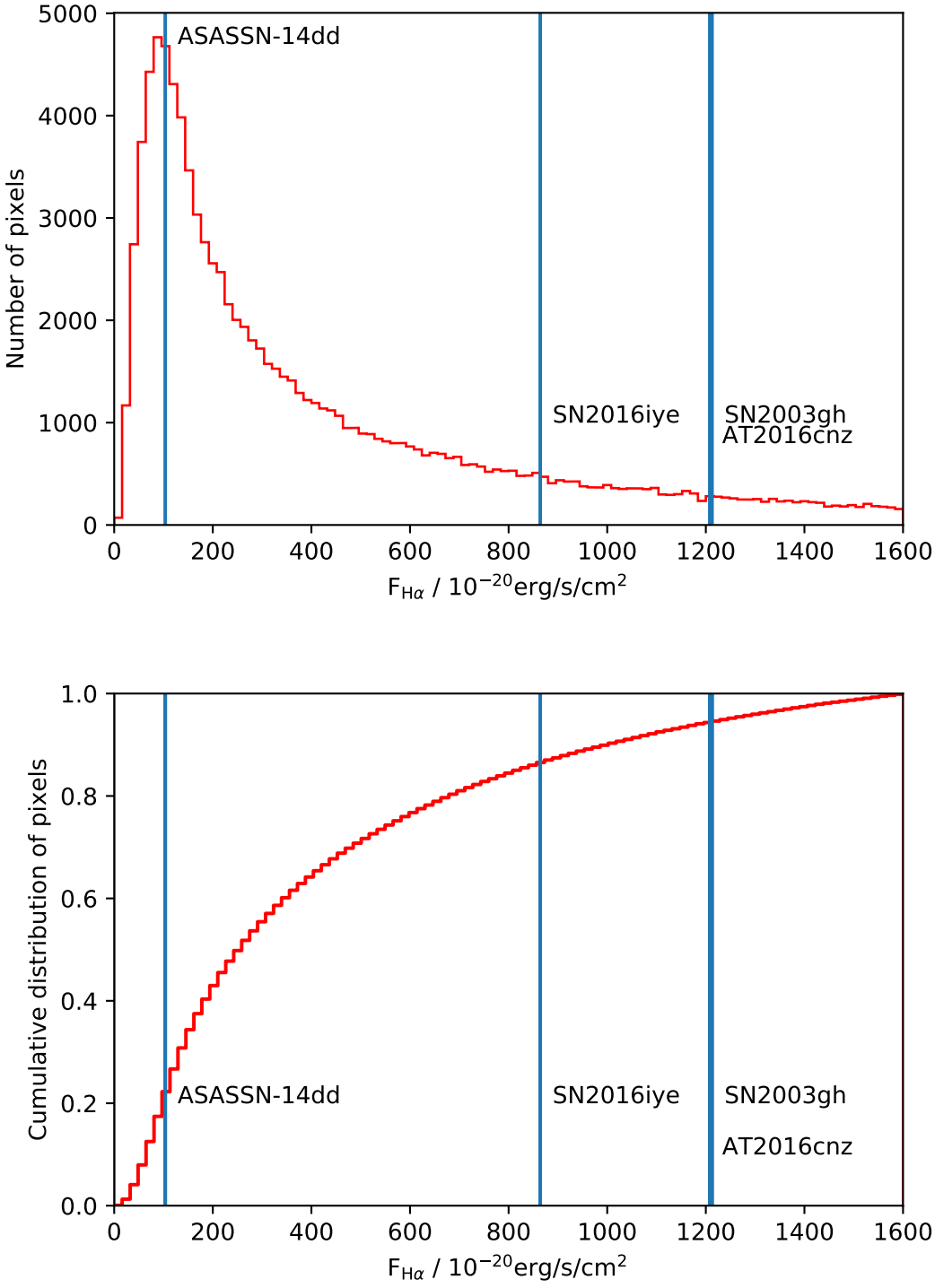

Figure 17. Distribution function and cumulative distribution of Hα flux pixels. High fraction of pixels are comparatively dim compared to the brightest pixels. The SN ASASSN-14dd is clearly situated in a dimmer part of the host galaxy and also in one of the most populated pixel bins.

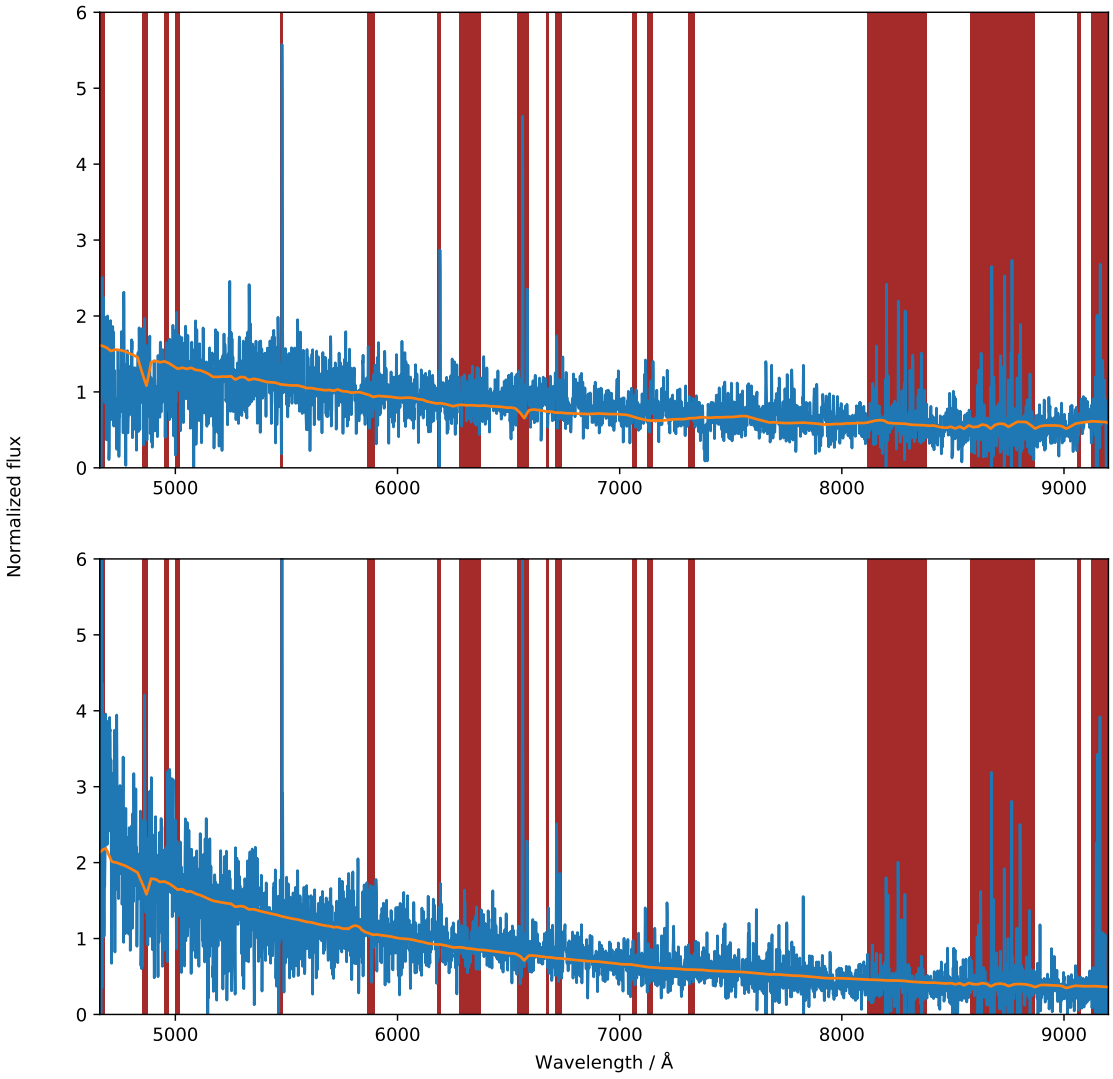

Figure 18. Extracted spectra (blue) of the supernova locations for ASASSN-14dd (top) and AT 2016cnz (bottom). Spectra are summed up spaxels from inside the PSF of the datacube, dereddened and shifted to restframe as described in Chapter 4. Overlaid is the best fit model spectra from BPASS (orange). Some of the wavelengths are masked (brown areas) during fitting due to telluric and nebular emission lines present in the spectra.

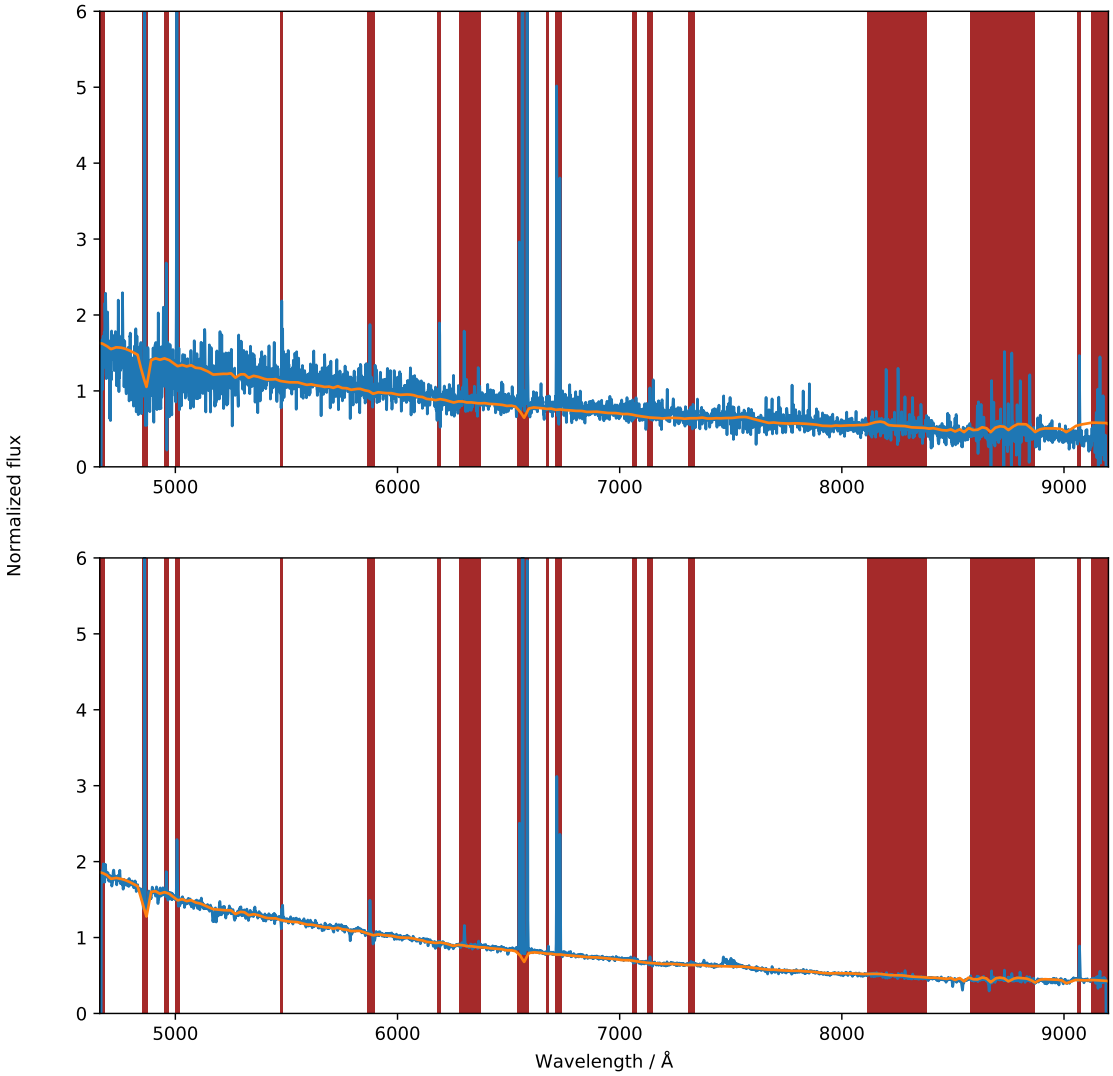

Figure 19. Extracted spectra (blue) of the supernova locations for SN 2016iye (top) and SN 2003gh (bottom). Spectra are summed up spaxels from inside the PSF of the datacube, dereddened and shifted to restframe wavelength as described in Chapter 4. Overlayed is the best fit model spectra from BPASS (yellow). Some of the wavelengths are masked (brown areas) during fitting due to telluric and nebular emission lines present in the spectra.

		ASASSN-14dd	AT 2016cnz
SN Type		Ibn	-
Right Ascension		7:45:14.38	7:45:22.97
Declination		-71:24:14.04	-71:24:40.70
Galactocentric distance	kpc	9.63	12.15
A_V	mag	0.44	1.32
V_J	mag	21.0	-
R_C	mag	>21.5	-
I_C	mag	>21.9	-
O3N2	12+log(O/H)	-	-
N2	12+log(O/H)	8.59 ± 0.16	8.53 ± 0.16
S2	12+log(O/H)	-	8.46 ± 0.12
log(U)		-3.29 ± 0.1	-3.68 ± 0.09
L(Hα)	10^{37} erg s^{-1}	4.83	2.56
SFR	10^{-3}M$_\odot$ yr^{-1}	0.38	0.20
EW(Hα)	Å	17.77	20.47
EW age (S99)	10^6 yr	9.86	7.41
EW age (BPASS)	10^6 yr	81.6	72.9
S99 age	10^6 yr	8.0	7.0
BPASS age	10^6 yr	31.6	20.0

Table 2. Measurements of the SN locations. A_v is the total extinction measured. V_J, R_C and I_C are magnitudes measured for the location. Log(U) is the ionisation parameter and L(Hα) is the Hα luminosity of the location. SFR is the star formation rate calculated from L(Hα). EW(Hα) is the measured equivalent width of Hα at the SN location. This value is used to measure the population age, EW age, using data from two different surveys. S99 and BPASS ages are the age estimations from the spectral continuum fitting.

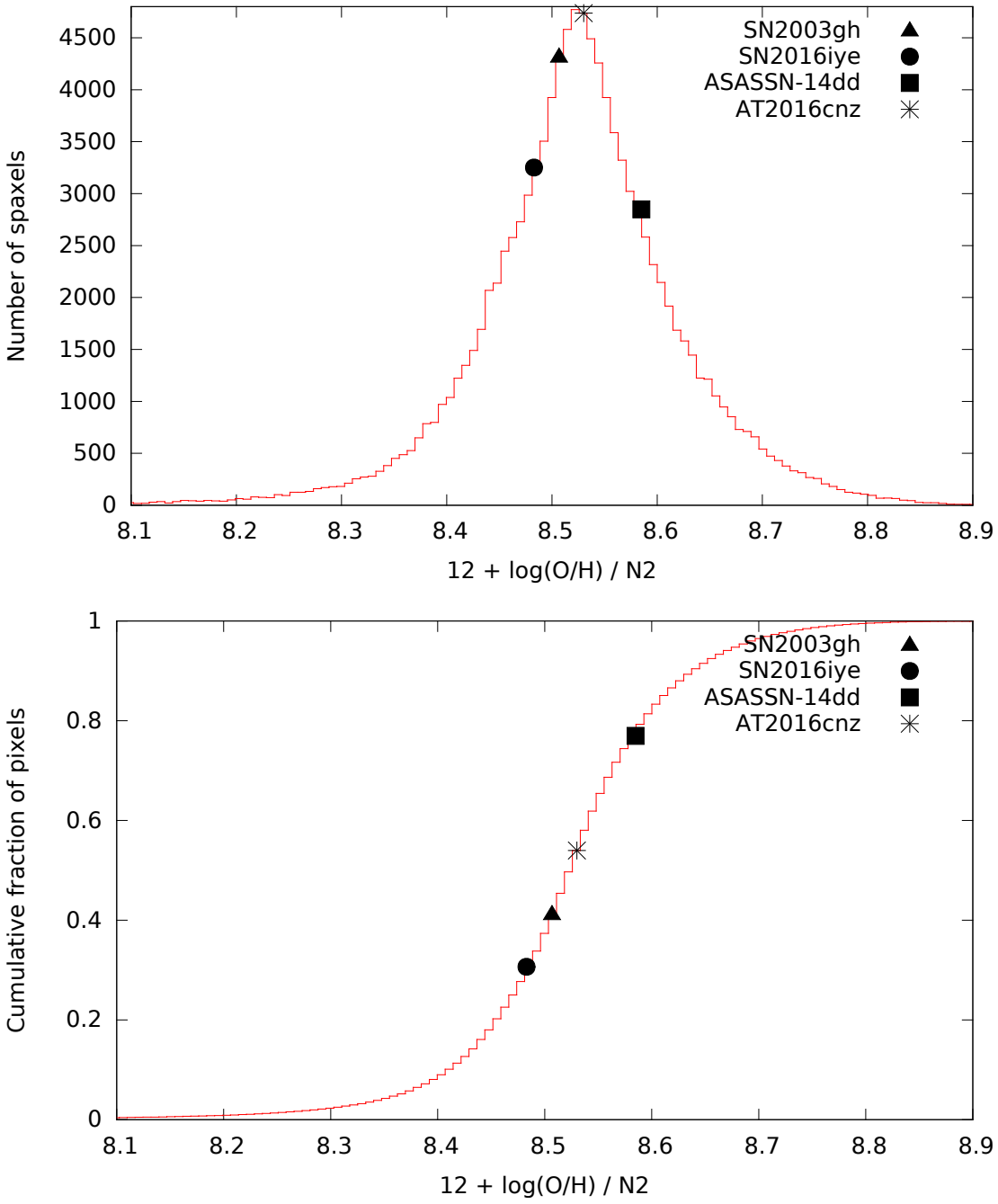

Figure 20. Distribution function and cumulative distribution of pixels with the N2 metallicity index. This is the only method that produces metallicity measurements for all four SNe regions.

is the lifetime of a 9-10$M_\odot$ star, which too small compared to the initial mass of $>25M_\odot$ required for a single WR star at near Solar metallicity.[69] This suggests the progenitor to be from a binary system. Even the mass given by Hα EW aging method with the measured EW of 17.8 Å is too low for a single component star system.

The SN location is between two large star-forming regions 2.4 kpc and 3.3 kpc away from the SN location. If the progenitor was an ejected WR star from one of these regions it would need a velocity of almost 470 km s^{-1} or 650 km s^{-1} to reach its explosion site in 5 Myr. Velocities higher than 500 km s^{-1} are improbable and velocities above 300 km s^{-1} rare. Typical ejection velocities for high mass stars are around 10-30 km/s making this scenario unlikely.[70, 71]

Hα luminosity is few times larger and the modelled age is an order of magnitude higher than Orion Nebula, indicating that the region is either larger than Orion Nebula or composed of several small nebulae that cannot be resolved as separate locations.[72] The estimated age for Orion Nebula is 2.5 Myr, so to observe similar Hα luminosities at higher ages the source needs to be larger to compensate the disappereance of massive stars. It is thus also possible that some small young star cluster is unobserved within the region that could still host WR stars, but the result still favour less massive and older progenitor.

BPASS binary evolution models can also be used to give constraints. The important parameters for the secondary are orbital period and the mass. Binary models in BPASS data show that to produce considerable helium envelope stripping but still have some left so as not to create a type Ic SN, the orbit needs to be less than few hundred days, but more than few days, for any secondary mass values. Most of the helium stripping happens in the last few hundred years in these models and the hydrogen stripping few million years before that.

5.4 AT 2016cnz

The transient had no follow-up observation after the original photometric detection, so there is no SN classification for it. Absolute magnitude in detection was -16.8 mag with a red filter and the last non-detection was a month before the transient observation.[1] The observed location coincides with an isolated, dim and spread out region in the dataset, likely a part of a broken arm structure. BPASS age estimation of 20 Myr suggests a CCSN and low metallicity makes a type II SN more likely, as suggested by the SN rates derived from the BPASS model (Table 2). A binary system type Ib SN is still not out of the question as these type of SNe are still occuring at ages of over 100 Myr in BPASS binary models.

5.5 SN 2016iye

The reported location of this type IIb SN is within one arcsec of the center of a bright H II region, likely a cluster of star-forming regions. It is possible that the SN is associated with this regions as a drift velocity of 17 km/s is enough for the progenitor to travel from the center of the nucleus to the current place in 20 Myrs. This is around a typical velocity dispersion in larger star clusters. [73]

Metallicity-wise the location is not particularly different from the galaxy. All of the diagnostics give a same value for the location, within their respective errors, and only the position on the host galaxy metallicity distribution changes between the diagnostics.

Fang et al. (2019)[74] note that the progenitor ZAMS mass for type IIb SN is inferred to be under 17 $M_\odot$ from observations. In these cases the progenitor has partially depleted hydrogen envelope with hydrogen masses less than 0.4 $M_\odot$. The initial mass is too low for a WR type star preventing the envelope stripping to be generated by stellar wind and argues for binary systems as the cause for it. The age

[1] https://wis-tns.weizmann.ac.il/object/2016cnz

estimations in Table 3 also point to binaries to be a more likely scenario. In BPASS binary models, stars with a thinned hydrogen envelope have mass range of 8-19 $M_{\odot}$. However, the initial mass and orbital period of the secondary star need to be tuned precisely in these scenarios as to not fully strip the primary of hydrogen.

5.6 SN 2003gh

The transient, a type Ia SN, is located within one of the primary spiral arms of the host galaxy. It is also the SN with the best S/N for its continuum spectrum in the MUSE datacube. The BPASS population age estimation of 50.1 Myr suggests that the region is currently not producing new stars en masse, but the EW measurements show that the arm is a location of very recent star formation. This is due to the assumption that the region only hosts one population of stars. In fact, the observed Hα luminosity can be produced by a host of smaller clusters that produce very little continuum emission compared to the large host of older stellar populations. Visually the continuum shows absorption lines of Hβ and CaII in the near-infrared end of the spectrum (cf. Appendix). These lines indicate that the spectrum is dominated by later type stars and demonstrates the older age of the population. This would indicate that the Hα EW of the star forming region in the spiral is actually even higher as the older population does not produce Hα emissions. This indicates that current star formation is happening in young regions that are contaminated by the older population in the continuum.

Pixel statistics of metallicity in Figures 20, 21 and 22 show increasing metallicity with newer metallicity indices. This SN region has the highest ionisation parameter and is affected the strongest by it. Especially with nearby observations this could affect even long-slit spectroscopy, if the observed H II region is large enough that outer parts of the region are cropped out from the observation. This could cause unwanted bias into statistical studies and observers should consider to account for

		SN 2016iye	SN 2003gh
SN Type		IIb	Ia
Right Ascension		7:45:19.72	7:45:17.93
Declination		-71:24:17.90	-71:24:37.3
Galactocentric distance	kpc	9.63	3.33
A_V	mag	0.87	1.46
V_J	mag	-	18.3
R_C	mag	-	19.6
I_C	mag	-	20.3
O3N2	12+log(O/H)	8.44 ± 0.18	8.59 ± 0.18
N2	12+log(O/H)	8.48 ± 0.16	8.51 ± 0.16
S2	12+log(O/H)	8.53 ± 0.12	8.75 ± 0.12
log(U)		-3.35 ± 0.1	-3.09 ± 0.11
L(Hα)	10^{37} erg s^{-1}	69.46	536.82
SFR	$10^{-3}M_\odot$ yr^{-1}	5.49	42.3
EW(Hα)	Å	97.15	73.54
EW age (S99)	10^6 yr	6.17	6.25
EW age (BPASS)	10^6 yr	15.1	18.0
S99 age	10^6 yr	8.0	8.0
BPASS age	10^6 yr	31.6	50.1

Table 3. Measurements of SN locations, similar to Table 2

the local ionisation parameter in the future.

If the SN is related to the population seen in the continuum, the age would coincide with one of the channels of Ia SNe. There might also be an undetected population of stars older than 1 Gyr. Because type Ia SN progenitors are old, the original cluster they formed in might have already dispersed and the progenitors migrated far away from the original location. The explosion site would then be unlikely to be associated with the SN itself.

5.7 Star formation and supernova activity in the host galaxy.

In absolute values both star formation and SN rate are heightened in the host galaxy when compared to a quiescent galaxy such as the Milky Way with SFR of about 1 $M_{\odot}$ and one or two expected SNe per century.[63, 75] However, galaxies come in highly different sizes so it is worthwhile to take into account the size of the host galaxy for better comparison. Diameter of the host galaxy is about 35 kpc when estimating from the MUSE FoV, which is of the same order as the size of the Milky Way.[76] This indicates that NGC 2466 is indeed undergoing higher than usual SFR compared to its size. Recently Eldridge and Xiao (2019)[77] estimated the SFR of NGC 6946, colloquially dubbed as "Fireworks Galaxy", indirectly from the frequency of recent SNe in it and derived a value of 12.1 $M_{\odot}yr^{-1}$, which is only double of NGC 2466. It is possible that NGC 2466 will be a host of future SNe in the coming years.

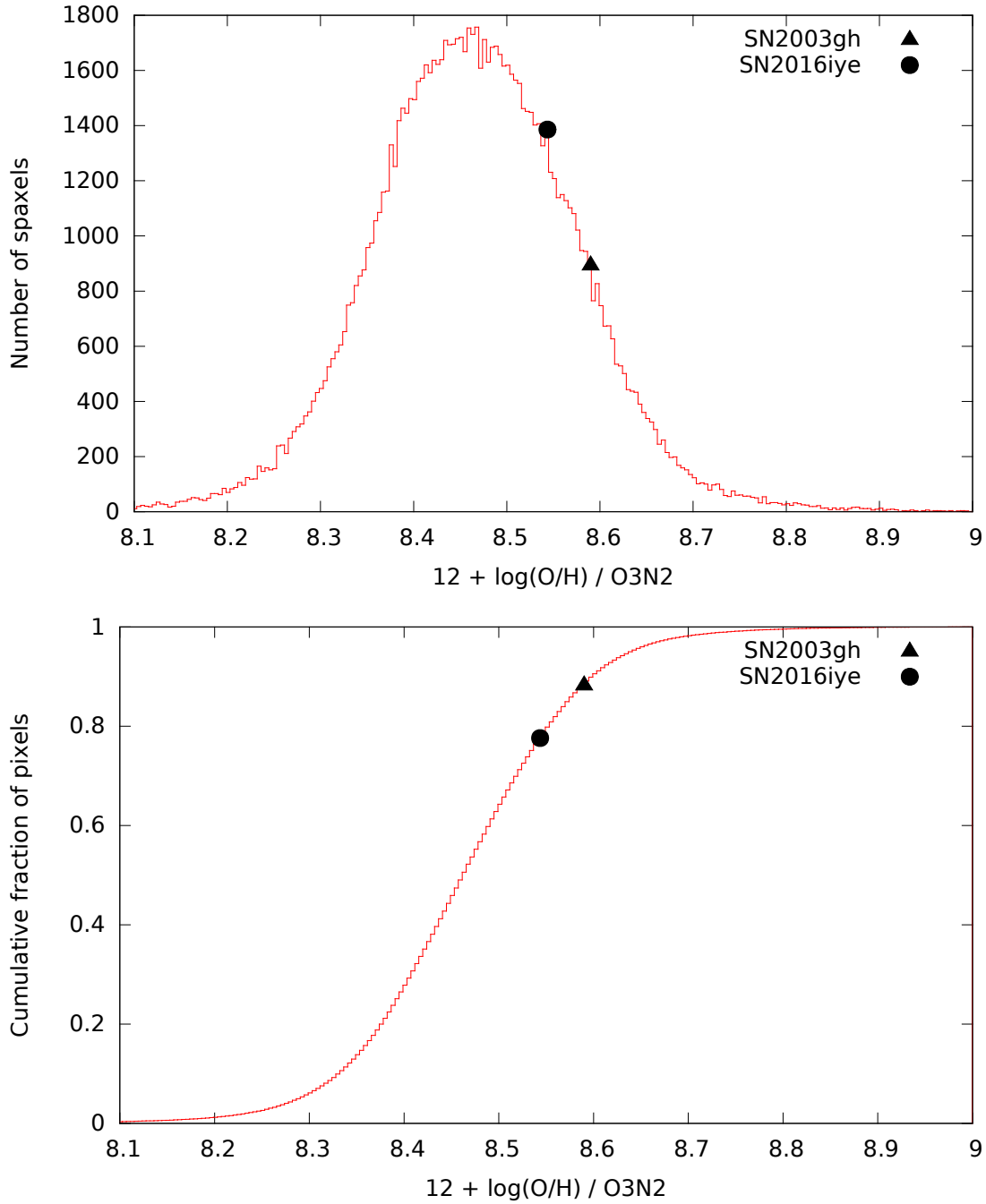

Figure 21. Distribution function and cumulative distribution of pixels with the O3N2 metallicity index. Only two of the SNe are measured, other SNe have missing emission line measurements. Both of the observed SN regions are in higher metallicity regions.

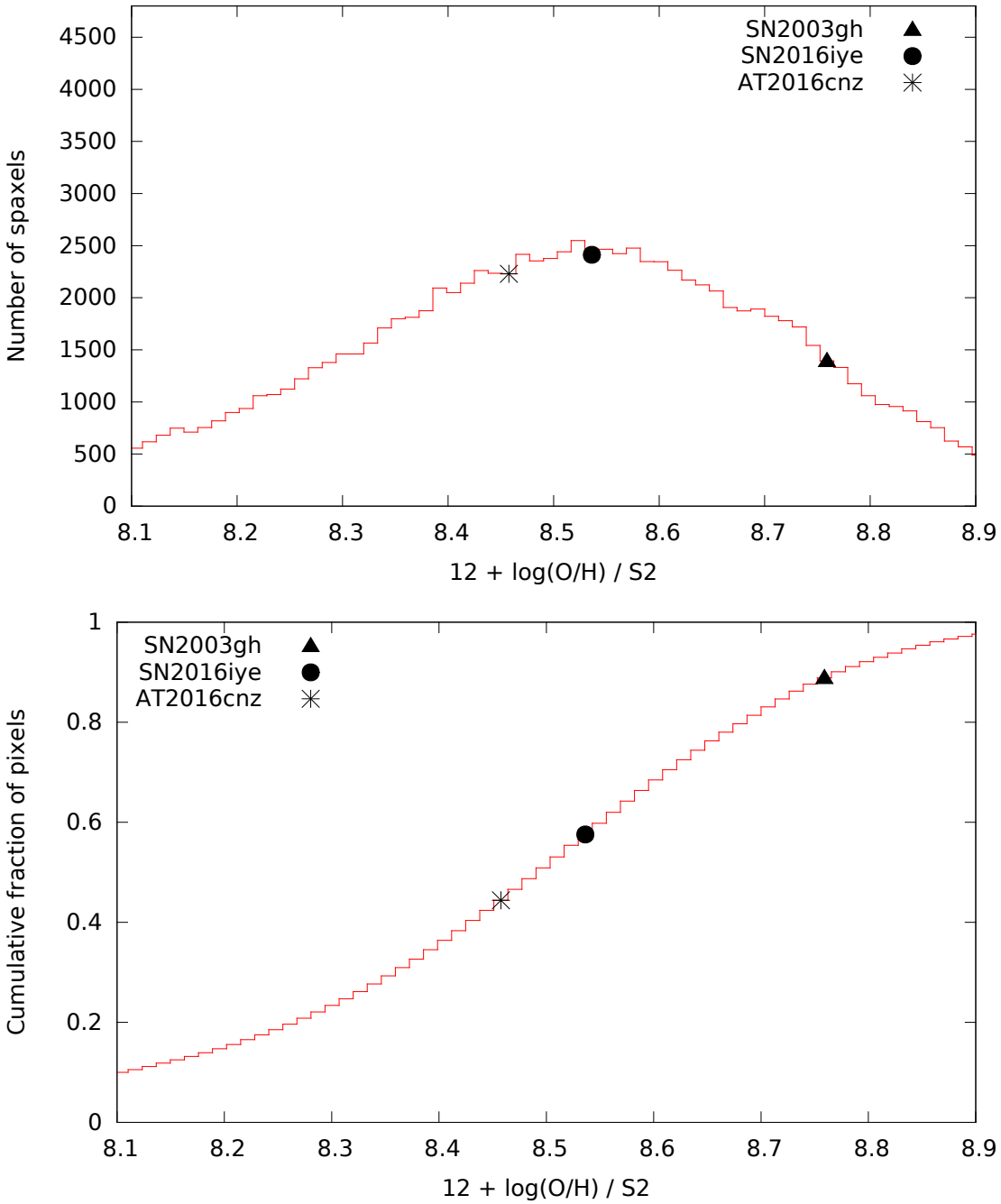

Figure 22. Distribution function and cumulative distribution of pixels with the S2 metallicity index.

6 Conclusions and future work

In this thesis I have studied the properties of the environments of the SNe and their host galaxy NGC 2466 as a whole. The aim was to constrain SN progenitors from the measurements of the metallicity and stellar population age in the local environments. CCSNe have a short lifespan, meaning that they are still co-located with the same stellar population they were born in. By comparing the parent stellar population spectra to those produced by stellar population evolution models the age of that population, and in turn the age of the SN progenitor, can be deduced. Age of a progenitor is directly linked to the initial mass of the progenitor, which governs the stellar evolution.

The SNe ASASSN-14dd (type Ibn), and SN 2016iye, (type IIb) in the galaxy were shown to likely originate from binary systems due to the relatively old age of the environment. Both SNe are relatively distant from the center of the host galaxy and located in H II regions, whose metallicity is consistent with observed metallicity gradient of the galaxy. This suggests that metallicity is not an important parameter for these SNe. The type Ia SN (SN 2003gh) was shown to have an environment with an age close to the lifetime of the heaviest stars that produce white dwarfs. Delay time from the emergence of the white dwarf progenitor to a SN explosion would then be short, only some tens of millions to couple hundred millions of years instead of couple billions of years. Therefore it is unlikely that the SN Ia progenitor is associated with the observed population. The unidentified transient, AT 2016cnz, in the galaxy provided an interesting case. Even though it does not have a spectral classification, the immediate region shows recent star formation activity and the transient could be a type II SN, but a spectral identification would have been needed for a positive identification due to the multiplicity of different SN types around that age.

As a continuation for this thesis it would be valuable to apply these methods

to a larger set of SNe of the given types. The degree of the role binary systems have on type Ibn SNe is still unknown, but with environmental studies this could be determined. Type Ibn SN environments are still not well studied and offer a great opportunity for new developments. Environmental studies therefore complement direct observations of SNe giving better constraints for the progenitors.

Statistical studies could also be extended to study the star system of SNe with binary system progenitors. While in this thesis I have used simple stellar populations to constrain the age of the progenitor, the star system models used to construct the population data itself would then have a second use. Orbital parameters could be constrained by studying models that reproduce observed variables such as mass or density of circumstellar shells. These new orbital constraints may then give clues to SN progenitor populations and their nature.

Acknowledgements

I would like to thank my supervisors Hanindyo Kuncarayakti and Seppo Mattila, without whose advice and support this thesis would not have been possible.

Based on observations made with ESO Telescopes at the La Silla Paranal Observatory under programme ID 096.D-0296. The computer resources of the Finnish IT Center for Science (CSC) and the FGCI project (Finland) are acknowledged. This research has also made use of the NASA/IPAC Extragalactic Database (NED) which is operated by the Jet Propulsion Laboratory, California Institute of Technology, under contract with the National Aeronautics and Space Administration.

References

[1] A. V. Filippenko, Annual Review of Astronomy and Astrophysics **35**, 309 (1997).

[2] N. Langer, Annual Review of Astronomy and Astrophysics **50**, 107 (2012).

[3] S.-C. Yoon, L. Dessart and A. Clocchiatti, The Astrophysical Journal **840**, 10 (2017).

[4] S. Mattila *et al.*, Monthly Notices of the Royal Astronomical Society **389**, 141 (2008).

[5] A. Pastorello *et al.*, Nature **447**, 829 (2007).

[6] N. Smith, R. J. Foley and A. V. Filippenko, The Astrophysical Journal **680**, 568 (2008).

[7] H. Kuncarayakti *et al.*, Astronomy & Astrophysics **613**, A35 (2018).

[8] X. Meng and W. Yang, Astrophysics and Space Science **329**, 287 (2010).

[9] T. Matheson *et al.*, The Astrophysical Journal **754**, 19 (2012).

[10] A. Odrzywolek and T. Plewa, Astronomy & Astrophysics **2**, 11 (2010).

[11] T. D. Brandt *et al.*, Astronomical Journal **140**, 804 (2010).

[12] N. Smith, W. Li, A. V. Filippenko and R. Chornock, Monthly Notices of the Royal Astronomical Society **412**, 1522 (2010).

[13] O. Pejcha and T. A. Thompson, The Astrophysical Journal **746**, 106 (2012).

[14] C. S. Kochanek, Monthly Notices of the Royal Astronomical Society **446**, 1213 (2015).

[15] S. J. Smartt, Annual Review of Astronomy and Astrophysics **47**, 63 (2009).

[16] P. Crowther and L. Hadfield, The Messenger **129**, 53 (2007).

[17] S. E. de Mink *et al.*, The Astrophysical Journal **764**, 166 (2013).

[18] H. Sana *et al.*, Science **337**, 444 (2012).

[19] H. Kuncarayakti *et al.*, The Astronomical Journal **146**, 30 (2013).

[20] S. J. Smartt, Science **303**, 499 (2004).

[21] S. D. Van Dyk, Philosophical Transactions of the Royal Society A: Mathematical, Physical and Engineering Sciences **375**, 20160277 (2017).

[22] S. J. Smartt, J. J. Eldridge, R. M. Crockett and J. R. Maund, Monthly Notices of the Royal Astronomical Society **395**, 1409 (2009).

[23] E. E. Salpeter, The Astrophysical Journal **121**, 161 (1955).

[24] I. Shivvers *et al.*, Monthly Notices of the Royal Astronomical Society **471**, 4381 (2017).

[25] J. J. Eldridge *et al.*, Monthly Notices of the Royal Astronomical Society **436**, 774 (2013).

[26] C. Leitherer *et al.*, The Astrophysical Journal Supplement Series **212**, 14 (2014).

[27] N. Bastian and S. P. Goodwin, Monthly Notices of the Royal Astronomical Society: Letters **369**, L9 (2006).

[28] H. Kuncarayakti *et al.*, The Astronomical Journal **146**, 31 (2013).

[29] J. P. Anderson and P. A. James, Monthly Notices of the Royal Astronomical Society **390**, 1527 (2008).

[30] T. Kangas *et al.*, Monthly Notices of the Royal Astronomical Society **436**, 3464 (2013).

[31] T. Kangas *et al.*, Astronomy & Astrophysics **597**, A92 (2017).

[32] L. Sánchez-Menguiano *et al.*, The Astrophysical Journal **830**, L40 (2016).

[33] T. Nugis and H. Lamers, Astronomy & Astrophysics **360**, 227 (2000).

[34] A. A. Hakobyan *et al.*, Astronomy & Astrophysics **508**, 1259 (2009).

[35] S. M. Habergham, P. A. James and J. P. Anderson, Monthly Notices of the Royal Astronomical Society **424**, 2841 (2012).

[36] G. Chauvin *et al.*, Astronomy & Astrophysics **573**, A127 (2015).

[37] L. Galbany *et al.*, Monthly Notices of the Royal Astronomical Society **455**, 4087 (2016).

[38] L. Sánchez-Menguiano *et al.*, Astronomy & Astrophysics **609**, A119 (2018).

[39] M. F. Skrutskie *et al.*, The Astronomical Journal **131**, 1163 (2006).

[40] M. J. Meyer *et al.*, Monthly Notices of the Royal Astronomical Society **350**, 1195 (2004).

[41] W. Freudling *et al.*, Astronomy & Astrophysics **559**, A96 (2013).

[42] J. J. Eldridge *et al.*, Publications of the Astronomical Society of Australia **34**, e058 (2017).

[43] R. Cid Fernandas *et al.*, Monthly Notices of the Royal Astronomical Society **358**, 363 (2005).

[44] M. Asplund *et al.*, Astronomy & Astrophysics **417**, 751 (2004).

[45] C. Leitherer and D. Shaerer, ApJ **123**, 1 (1999).

[46] J. A. Cardelli, G. C. Clayton and J. S. Mathis, The Astrophysical Journal **345**, 245 (1989).

[47] D. Calzetti *et al.*, The Astrophysical Journal **533**, 682 (2000).

[48] E. F. Schlafly and D. P. Finkbeiner, The Astrophysical Journal **737**, 103 (2011).

[49] D. J. Schlegel, D. P. Finkbeiner and M. Davis, The Astrophysical Journal **500**, 525 (1998).

[50] A. Domínguez *et al.*, The Astrophysical Journal **763**, 145 (2013).

[51] D. Osterbrock, *Astrophysics of gaseous nebulae and active galactic nuclei* (University Science Books,Mill Valley, CA, 1989), p. 422.

[52] R. C. Kennicutt, Annual Review of Astronomy and Astrophysics **36**, 189 (1998).

[53] E. Zapartas *et al.*, Astronomy & Astrophysics **601**, A29 (2017).

[54] L. Xiao, J. J. Eldridge, E. Stanway and L. Galbany, Proceedings of the International Astronomical Union **12**, 49 (2016).

[55] S. C. C. Yeh and C. D. Matzner, Astrophysical Journal **757**, 1 (2012).

[56] A. I. Díaz *et al.*, Monthly Notices of the Royal Astronomical Society **253**, 245 (1991).

[57] C. Mendoza and C. J. Zeippen, Monthly Notices of the Royal Astronomical Society **199**, 1025 (1982).

[58] J. L. Dors, A. Krabbe, G. F. Hägele and E. Pérez-Montero, Monthly Notices of the Royal Astronomical Society **415**, 3616 (2011).

[59] B. E. J. Pagel *et al.*, Monthly Notices of the Royal Astronomical Society **189**, 95 (1979).

[60] R. A. Marino *et al.*, Astronomy & Astrophysics **559**, A114 (2013).

[61] M. A. Dopita, L. J. Kewley, R. S. Sutherland and D. C. Nicholls, Astrophysics and Space Science **361**, 61 (2016).

[62] S. Rahmani, S. Lianou and P. Barmby, Monthly Notices of the Royal Astronomical Society **456**, 4128 (2016).

[63] T. P. Robitaille and B. A. Whitney, The Astrophysical Journal **710**, L11 (2010).

[64] D. Richardson, R. L. Jenkins III, J. Wright and L. Maddox, The Astronomical Journal **147**, 118 (2014).

[65] A. Pastorello *et al.*, Monthly Notices of the Royal Astronomical Society **389**, 955 (2008).

[66] C. Kehrig *et al.*, Monthly Notices of the Royal Astronomical Society **432**, 2731 (2013).

[67] T. Krühler *et al.*, Astronomy & Astrophysics **602**, A85 (2017).

[68] J. P. Anderson and P. A. James, Monthly Notices of the Royal Astronomical Society **399**, 559 (2009).

[69] A. Bressan, Space Science Reviews **66**, 373 (1994).

[70] M. D. Silva and R. Napiwotzki, Monthly Notices of the Royal Astronomical Society **411**, 2596 (2011).

[71] S. Oh and P. Kroupa, Astronomy & Astrophysics **590**, A107 (2016).

[72] R. D. Jeffries, S. P. Littlefair, T. Naylor and N. J. Mayne, Monthly Notices of the Royal Astronomical Society **418**, 1948 (2011).

[73] N. McCrady and J. R. Graham, The Astrophysical Journal **663**, 844 (2007).

[74] Q. Fang *et al.*, Nature Astronomy **3**, 434 (2019).

[75] T. C. Licquia and J. A. Newman, The Astrophysical Journal **806**, 96 (2015).

[76] M. López-Corredoira *et al.*, Astronomy & Astrophysics **612**, L8 (2018).

[77] J. J. Eldridge and L. Xiao, Monthly Notices of the Royal Astronomical Society: Letters **485**, L58 (2019).